Structural and Multidisciplinary Optimization (2022) 65:254
https://doi.org/10.1007/s00158-022-03320-y

RESEARCH PAPER

Limiting the first principal stress in topology optimization: a local and consistent approach

Oliver Giraldo-Londoño[1] · **Jonathan B. Russ**[2,3] · **Miguel A. Aguiló**[4,5] · **Glaucio H. Paulino**[2,3]

Received: 2 March 2022 / Revised: 21 June 2022 / Accepted: 23 June 2022
© The Author(s), under exclusive licence to Springer-Verlag GmbH Germany, part of Springer Nature 2022

Abstract
The present study introduces a formulation for topology optimization of structures with constraints on the first principal stress. We solve the problem considering local stress constraints via the augmented Lagrangian method, which enables the solution of large-scale problems without the need for ad hoc aggregation schemes and clustering methods. Numerical examples are provided which demonstrate the effectiveness of the framework for practical problems with numerous (e.g., in the range of million(s)) local constraints imposed on the maximum principal stress. One of the examples is a three-dimensional antenna support bracket, which represents a realistic engineering design problem. This example, which has more than one million constraints, is proposed as a benchmark problem for stress-constrained topology optimization.

Keywords Local stress constraints · Topology optimization · Augmented Lagrangian · Principal stresses

1 Introduction

In engineering practice, it is hard to overstate the complexity of the design problems that are often confronted throughout many different industries. Frequently, large teams of talented and creative experimentalists, analysts, and designers are required to produce an initial design candidate and progressively refine it into a product which meets a large collection of requirements. While this is obviously a complex task for assemblies like an aircraft, it is also true for the lower level components of such systems where it might be initially surprising to discover an exceptional degree of difficulty. The number of different scenarios and physics which must be considered during the design process generally renders the task unachievable when armed with only human intuition and analytical methods. While there are multiple design methods that attempt to address this issue, topology optimization has become increasingly successful in this regard and seems to hold a great deal of future promise. Born in the minds of two great scientists more than three decades ago (Bendsøe and Kikuchi 1988), the mathematical beauty of the method might only be outdone by its increasingly apparent utility in practice.

However, as with most mathematical techniques in engineering, topology optimization was quickly confronted with numerous challenges. Perhaps most importantly, design for avoiding structural failure became the focus of much of the literature as the difficulty and practical interest in solving the problem became evident. While there are multiple ways in which one might account for structural failure during the design process, the imposition of local constraints (typically on stress-related criteria) has drawn much of the attention. Multiple challenges of such a strategy have been discovered and are noted in many prior works, which are nicely summarized in Bendsøe and Sigmund (2003); Sigmund and Maute (2013); Deaton and Grandhi (2014), for example. These include the so-called singularity phenomenon, which is now typically resolved via constraint relaxation techniques (Cheng and Guo 1997; Rozvany 2001; Bruggi

Responsible Editor: Ole Sigmund

✉ Oliver Giraldo-Londoño
ogiraldo@missouri.edu

[1] Department of Civil and Environmental Engineering, University of Missouri, Columbia, MO 65211, USA

[2] Department of Civil and Environmental Engineering, Princeton University, Princeton, NJ 08544, USA

[3] Princeton Institute for the Science and Technology of Materials (PRISM), Princeton University, Princeton, NJ 08544, USA

[4] Simulation and Modeling Sciences, Sandia National Laboratories, Albuquerque, NM 87185, USA

[5] Morphorm LLC, Albuquerque, NM 87102, USA

Published online: 27 August 2022

2008). However, an additional issue arises due to the local nature of stress and the potentially huge number of constraints that must be imposed; typically one for each element or integration point in the finite element discretization. This problem is significantly compounded for practical engineering design in which multiple load cases must often be considered and dynamic analyses may also be required. Constraining a local stress measure for multiple load cases or at each step of a potentially dynamic analysis can easily result in many millions of stress constraints for practical problems. While the vast majority of the existing literature has resorted to constraint aggregation and clustering schemes (Yang and Chen 1996; Duysinx and Sigmund 1998; Bendsøe and Sigmund 2003; Paris et al. 2009, 2010; Le et al. 2010), it seems increasingly unlikely that these methods will become computationally tractable for practical engineering design in which large finite element meshes, multiple load cases, and dynamic analyses (generally composed of many time increments) are required. In contrast to global approaches, local strategies based on the augmented Lagrangian (AL) method (Bertsekas 1996, 1999; Nocedal and Wright 2006) have demonstrated the ability to handle millions of local constraints and inherently respect the local nature of stress as proposed by Cauchy nearly two centuries ago (Cauchy 1827). Pereira et al. (2004) have employed the AL method for imposing stress constraints in the context of density-based topology optimization, which is a concept that has been further explored and expanded in recent works (Giraldo-Londoño and Paulino 2020; da Silva et al. 2021).

The majority of the existing stress-constrained topology optimization works in the literature have considered constraints on the von Mises stress measure, although it is typically only appropriate for structural design with materials akin to ductile metals. A level set formulation with Drucker-Prager type stress constraints was proposed by Amstutz et al. (2012). Additionally, Luo and Kang (2012) also employed the Drucker-Prager criterion for materials with different strengths in tension and compression. Similar formulations were unified by Giraldo-Londoño and Paulino (2020) using a single failure surface encompassing several classical failure criteria, including von Mises, Tresca, Drucker-Prager, and Mohr-Coulomb, among others. However, for isotropic, brittle engineering materials failure may be more appropriately prevented by constraining the maximum principal stress in the structure. Surprisingly, there are very few existing works which directly address this important application. Recently, Chen et al. (2021) proposed a BESO formulation for constraining the maximum principal stress. In their work, the largest maximum principal stress in the domain is approximated using a p-norm type aggregation function which is constrained to be below a user-specified upper bound. Numerical examples with fewer than 50,000 elements are then provided, along with results obtained taking differing values of the p-norm parameter, "p." Additionally, Holmberg et al. (2014) considered the largest tensile principal stress in the context of fatigue in which a p-norm strategy was also employed, along with a clustering technique in order to improve the approximation of the local stresses. However, results are provided for numerical examples which do not include more than 7000 elements.

In the current work, we propose the use of the AL method for imposing local constraints on the maximum principal stress, which enables the solution of the original problem with local stress constraints using a mathematically well-established formulation while also allowing larger practical problems to be considered. Additionally, due to the tension–compression asymmetry of such a criterion, we propose the use of an aggregate objective function including the compliance as a computationally efficient means of adding support for compression-dominated structural members. The calculation of the first principal stress is also performed efficiently using an easily vectorized form (both in 2D and 3D) in order to take advantage of shared-memory parallelism. Finally, we note that the AL formulation does not require the special treatment of a negative first principal stress, as is addressed using a Heaviside function within the p-norm aggregation function in Chen et al. (2021), for example.

The remainder of the paper is organized as follows: In Sect. 2, the details of the mathematical optimization problem statement are provided. Subsequently, the augmented Lagrangian formulation for imposing the local stress constraints is presented in Sect. 3 and multiple numerical examples are provided in Sect. 4. In contrast to previous works, principal stress based design results are provided for examples in which millions of constraints must be enforced, demonstrating the ability of the method to be used in practice where large finite element models are frequently encountered. One of the examples consists of a 3D antenna support bracket with more than a million stress constraints, which is proposed as a benchmark in the field of stress-constrained topology optimization. In Sect. 5 we offer a few concluding remarks, after which we provide four appendices. Appendix 1 contains the details of the sensitivity analysis, convergence plots for select examples are shown in Appendix 2, the formulation is extended to also include compressive principal stress constraints in Appendix 3, and Appendix 4 contains the nomenclature used in the present study.

2 Stress-constrained formulation

The formulation introduced herein seeks to minimize an objective function, $f(\mathbf{z}, \mathbf{u})$, with constraints, $g_j(\mathbf{z}, \mathbf{u}) \leq 0$, used to limit the first principal stresses at the centroid of each element, j, with $j = 1, \ldots, N$. The topology is represented as a function of the design variable vector, $\mathbf{z} \in [0,1]^N$, and the displacement field, $\mathbf{u}$, is obtained from the solution of the linear equilibrium equation $\mathbf{Ku} = \mathbf{f}$, where $\mathbf{K}$ and $\mathbf{f}$ are the global stiffness matrix and load vector, respectively.[1] The formulation described above is formally written as follows:

$$\begin{aligned} &\min_{\mathbf{z}\in[0,1]^N} \quad f(\mathbf{z},\mathbf{u}) \\ &\quad \text{s.t.} \quad g_j(\mathbf{z},\mathbf{u}) \le 0, \quad j = 1,\dots,N \\ &\quad \text{with:} \quad \mathbf{Ku} = \mathbf{f}. \end{aligned} \tag{1}$$

This formulation is valid for any objective function, $f(\mathbf{z},\mathbf{u})$, but in particular, we define f as a weighted sum of the mass ratio and the mean compliance.[2] That is,

$$f(\mathbf{z},\mathbf{u}) = (1-w)\overline{m}(\mathbf{z}) + w\overline{C}(\mathbf{u}), \quad 0 \le w \le 1 \tag{2}$$

where:

$$\overline{m}(\mathbf{z}) = \frac{\mathbf{A}^T\mathbf{V}}{\mathbf{A}^T\mathbf{V}_0} \quad \text{and} \quad \overline{C}(\mathbf{u}) = \frac{\mathbf{f}^T\mathbf{u}}{\mathbf{f}^T\mathbf{u}_0}. \tag{3}$$

The function $\overline{m}(\mathbf{z})$ is the volume of the structure normalized by its initial volume and $\overline{C}(\mathbf{u})$ is the mean compliance normalized by the initial mean compliance. In addition, $\mathbf{A} = \{|\Omega_\ell|\}_{\ell=1}^N$ is a vector of element areas (2D) or volumes (3D), where Ω_ℓ defines the domain for element ℓ, and $\mathbf{V} = m_V(\mathbf{y})$ is a vector of volume fractions obtained using the threshold projection function (Wang et al. 2011):

$$m_V(y_\ell) = \frac{\tanh(\bar{\beta}\bar{\eta}) + \tanh(\bar{\beta}(y_\ell - \bar{\eta}))}{\tanh(\bar{\beta}\bar{\eta}) + \tanh(\bar{\beta}(1-\bar{\eta}))}, \tag{4}$$

where $\bar{\beta}$ controls the aggressiveness of the projection, $\bar{\eta}$ is the threshold projection density, and $\mathbf{y} = \mathbf{Pz}$ is the vector of filtered densities, in which $\mathbf{P}$ is the filter matrix:

$$P_{ij} = \frac{w_{ij}A_j}{\sum_{k=1}^N w_{ik}A_k}, \quad \text{with} \quad w_{ij} = \max\left(0, 1 - \frac{\|\mathbf{x}_i - \mathbf{x}_j\|_2}{R}\right)^q, \tag{5}$$

where $\|\mathbf{x}_i - \mathbf{x}_j\|_2$ is the distance between the centroids of elements i and j, respectively, R is the filter radius, and q is the filter exponent.

The stiffness matrix is obtained as

$$\mathbf{K} = \sum_{\ell=1}^N E_\ell \mathbf{k}_\ell, \quad \text{with} \quad \mathbf{k}_\ell = \int_{\Omega_\ell} \mathbf{B}_\ell^T \mathbf{D}_0 \mathbf{B}_\ell \mathrm{d}\mathbf{x}, \tag{6}$$

where $\sum_{\ell=1}^N$ is the FE assembly operator, $\mathbf{k}_\ell$ is the element stiffness matrix, $\mathbf{D}_0$ is the material moduli matrix of the solid material, $\mathbf{B}_\ell$ is the strain–displacement matrix, and $E_\ell = m_E(y_\ell)$, where

$$m_E(y_\ell) = \epsilon + (1-\epsilon)m_V(y_\ell)^p \tag{7}$$

is the SIMP interpolation function (referred to as stiffness interpolation function in this work) modified by an Ersatz parameter, $\epsilon \ll 1$.[3]

2.1 Stress constraint definition

The present formulation imposes constraints on the maximum principal stress to prevent the tensile stresses in the optimized designs from exceeding a given threshold, $\sigma_{\lim}$. We define the stress constraints using the *polynomial vanishing constraint* (Giraldo-Londoño and Paulino 2020), as follows:

$$g_j(\mathbf{z},\mathbf{u}) = E_j\Lambda_j(\Lambda_j^2 + 1) \le 0, \quad j = 1,\dots,N, \tag{8}$$

where

$$\Lambda_j = \sigma_j^1/\sigma_{\lim} - 1, \tag{9}$$

and σ_j^1 is the first principal stress at the centroid of element j. Function Λ_j is in essence a failure function based on the first principal stress.

We compute the first principal stress as follows:[4]

$$\sigma_1 = \frac{2}{\sqrt{3}}\sqrt{J_2}\sin(\theta + 2\pi/3) + \frac{I_1}{3} \tag{10}$$

---

[1] Although crack initiation in brittle materials typically occurs at stress concentrations arising near material defects, we assume the material is isotropic and homogeneous for simplicity. In practice, this simplification might be addressed via typical engineering safety factors placed on the selected stress limit, or via optimization under uncertainty methods accounting for spatially varying material properties such as the elastic modulus and/or stress limit.

[2] One important difficulty that arises when trying to solve mass minimization problems with maximum principal stress constraints, as opposed to von Mises, is the lack of active constraints in compression-dominated regions of the domain. Although these regions are often necessary for satisfying the local constraints elsewhere in the structure, only the filter radius generally prevents them from becoming overly thin, as mentioned later in Sect. 4.1. Additionally, for the numerical examples we have tested, the optimization problem often requires more iterations to converge when compared with a problem based on von Mises stress constraints. Adding the compliance to the objective is a simple, computationally efficient strategy for mitigating some of the aforementioned difficulty since it not only provides support for compression-dominated structural members but also has a stabilizing effect on the evolution of the structural topology.

[3] We use the Ersatz parameter to avoid numerical instabilities when $y_\ell \to 0$.

[4] This way of writing the first principal stress is consistent with the notation used by Giraldo-Londoño and Paulino (2020) in Eq. (3.1). In particular, the failure function based on the first principal stress, as shown in (9)–(10), is a particular case of the unified failure function by Giraldo-Londoño and Paulino (2020) with parameters $A = 2/3\sigma_{\lim}$, $B = 0$, $C = 1$, $D = 0$, $E = 0$, $\zeta = 1$, $\bar{\theta} = \pi/6$, $\hat{\beta} = 1/3\sigma_{\lim}$, and $\hat{\gamma} = 0$.

where I_1 is the first invariant of the Cauchy stress tensor, $\boldsymbol{\sigma}$, J_2 is the second invariant of the deviatoric stress tensor, $\mathbf{s}$, and

$$\theta = \frac{1}{3}\sin^{-1}\left(-\frac{3\sqrt{3}}{2}\frac{J_3}{J_2^{3/2}}\right), \quad -\pi/6 \le \theta \le \pi/6 \tag{11}$$

is the Lode angle[5], where $J_3 = \det(\mathbf{s})$ is the third invariant of the deviatoric stress tensor. Since the eigenvalues of the stress tensor are not obtained via a local iteration and there is no need to sort the eigenpairs, (10) may be trivially vectorized, leading to increased numerical efficiency, especially in 3D. Note that this form also enables elegant computation of the other two principal stresses in terms of the tensor invariants, which might be useful in the event the designer wishes to also constrain the minimum principal stress, σ_3. Although this work is focused on brittle materials which are generally limited by tensile stresses, for the convenience of the reader, we provide these additional relations below, where we have $\sigma_1 \ge \sigma_2 \ge \sigma_3$. A single example also constraining the minimum principal stress is included in Appendix 3 for the reader's convenience.

$$\sigma_2 = \frac{2}{\sqrt{3}}\sqrt{J_2}\sin(\theta) + \frac{I_1}{3} \tag{12}$$

$$\sigma_3 = \frac{2}{\sqrt{3}}\sqrt{J_2}\sin(\theta - 2\pi/3) + \frac{I_1}{3} \tag{13}$$

The first invariant of the Cauchy stress tensor is computed as

$$I_1 = \overline{\mathbf{M}}\boldsymbol{\sigma} \tag{14}$$

where $\overline{\mathbf{M}} = [1\ 1\ 0]$ and $\boldsymbol{\sigma} = [\sigma_{11}\ \sigma_{22}\ \sigma_{12}]^T$ for 2D problems, and $\overline{\mathbf{M}} = [1\ 1\ 1\ 0\ 0\ 0]$ and $\boldsymbol{\sigma} = [\sigma_{11}\ \sigma_{22}\ \sigma_{33}\ \sigma_{23}\ \sigma_{13}\ \sigma_{12}]^T$ for 3D problems. Similarly, the second invariant of the deviatoric stress tensor is computed as

$$J_2 = \frac{1}{3}\boldsymbol{\sigma}^T\overline{\mathbf{V}}\boldsymbol{\sigma} \tag{15}$$

where

$$\overline{\mathbf{V}} = \begin{bmatrix} 1 & -1/2 & 0 \\ -1/2 & 1 & 0 \\ 0 & 0 & 3 \end{bmatrix}$$

for 2D problems and

$$\overline{\mathbf{V}} = \begin{bmatrix} 1 & -1/2 & -1/2 & 0 & 0 & 0 \\ -1/2 & 1 & -1/2 & 0 & 0 & 0 \\ -1/2 & -1/2 & 1 & 0 & 0 & 0 \\ 0 & 0 & 0 & 3 & 0 & 0 \\ 0 & 0 & 0 & 0 & 3 & 0 \\ 0 & 0 & 0 & 0 & 0 & 3 \end{bmatrix}$$

for 3D problems.

The vector of Cauchy stress values (in Voigt notation) at the centroid of element j is computed as

$$\boldsymbol{\sigma}_j = \mathbf{D}_0\mathbf{B}_j\mathbf{u}_j, \tag{16}$$

where $\mathbf{u}_j$ is the displacement vector of element j and $\mathbf{B}_j$ is the strain–displacement matrix at the centroid of element j. Note that we compute $\boldsymbol{\sigma}_j$ using the elastic properties of the solid material (given by matrix $\mathbf{D}_0$), which means that the stress values used to evaluate the stress constraints (8) are unrelaxed. Unlike traditional approaches that typically use relaxed stresses, this way of defining the stress constraints allows obtaining solutions on an unrelaxed solution space (Giraldo-Londoño and Paulino 2020, 2021).

The third invariant of the deviatoric stress tensor is given by

$$J_3 = \frac{1}{3}I_1\left(J_2 - \frac{1}{9}I_1^2\right) \tag{17}$$

for 2D problems and by

$$J_3 = s_{11}s_{22}s_{33} + 2\sigma_{23}\sigma_{13}\sigma_{12} - (s_{11}\sigma_{23}^2 + s_{22}\sigma_{13}^2 + s_{33}\sigma_{12}^2) \tag{18}$$

for 3D problems, where $s_{ij}, i,j = 1,\dots,3$ are the components of the deviatoric stress tensor.

3 Solution via the augmented Lagrangian method

Based on our previous work (Giraldo-Londoño and Paulino 2020, 2021), we solve the optimization problem (1) via the AL method. That is, we solve (1) as a sequence of optimization problems aiming to minimize the AL of the problem. Specifically, at each step k of the AL method, we solve the following minimization problem:

$$\min_{\mathbf{z}\in[0,1]^N} J^{(k)}(\mathbf{z},\mathbf{u}) = f(\mathbf{z},\mathbf{u}) + \frac{1}{N}\sum_{j=1}^{N}\left[\lambda_j^{(k)}h_j(\mathbf{z},\mathbf{u}) + \frac{\mu^{(k)}}{2}h_j(\mathbf{z},\mathbf{u})^2\right], \tag{19}$$

where

$$h_j(\mathbf{z},\mathbf{u}) = \max\left(g_j(\mathbf{z},\mathbf{u}), -\frac{\lambda_j^{(k)}}{\mu^{(k)}}\right), \tag{20}$$

---

[5] To mitigate the unlikely event of a purely hydrostatic stress state, numerically one might compute the Lode angle as

$$\theta = \frac{1}{3}\sin^{-1}\left(-\frac{3\sqrt{3}}{2}\frac{J_3}{J_2^{3/2} + \epsilon_m}\right),$$

where $\epsilon_m \approx 2.2 \times 10^{-16}$ is on the order of machine epsilon.

$$\lambda_j^{(k+1)} = \lambda_j^{(k)} + \mu_j^{(k)} h_j(\mathbf{z}^{(k)}, \mathbf{u}), \text{ and} \tag{21}$$

$$\mu^{(k+1)} = \min\left(\alpha\mu^{(k)}, \mu_{\max}\right), \ \alpha > 1. \tag{22}$$

Parameters $\lambda_j^{(k)}$ and $\mu^{(k)}$ are, respectively, the Lagrange multiplier estimators and quadratic penalty term at the k-th step of the augmented Lagrangian method (Nocedal and Wright 2006). Based on our previous studies, $\lambda_j^{(1)} = 0$ and $\mu^{(1)} = 10$, $\mu_{\max} = 10,000$, and $\alpha = 1.1$ are suitable to solve static problems. The upper limit, $\mu_{\max}$, in (22) is chosen to prevent ill-conditioning.

The AL approach discussed herein is fundamentally different from typical approaches based on constraint aggregation techniques, which use smooth approximations of the maximum function to estimate the maximum stress in the design domain (e.g., see Le et al. 2010; Lee et al. 2012; Luo et al. 2013; Holmberg et al. 2013; Xia et al. 2018). In contrast to solutions based on the aggregation approaches just described, a solution obtained from the sequence of minimization problems (19) is expected to converge to the solution of the original optimization problem with local stress constraints (1) (e.g., see Bertsekas 1996, 1999; Nocedal and Wright 2006). Moreover, the normalization factor $1/N$ used in (19) has demonstrated to be an effective means of achieving nearly mesh-independent solutions (Giraldo-Londoño and Paulino 2021).

Finally, we note that the formulation extends to multiple load cases in a clear manner with an associated Lagrange multiplier estimator and penalty term for each element and each load case. No additional ad hoc decision must be made with regards to constraint aggregation or the quantity of constraints for the optimizer to explicitly impose. In this case, the summation in (19) is performed over the total number of constraints, which will equal the product of the number of elements, N, and the number of load cases considered, M. The normalization factor may then be updated to $1/(N \times M)$, which is a simple generalization of the $1/N$ factor previously mentioned.

4 Results and discussion

In this section, we present the results from six numerical examples which demonstrate the efficacy of the proposed formulation, both in two and three space dimensions. For select examples, results are provided with various weighting factors, w, on the volume fraction and compliance (2) in order to demonstrate the relevant trade-off between the two objectives. The compliance values reported in this section are all provided in units of kN-m. Additionally, the reported values of $m(\mathbf{z}^*)$ represent the unnormalized volume fraction rather than the normalized function, $\overline{m}(\mathbf{z})$, defined in (3). The stress maps shown in all numerical examples correspond to the normalized principal stress, $\widetilde{\sigma}_\ell^1 = E_\ell \sigma_\ell^1/\sigma_{\text{lim}}$, where $E_\ell = m_E(y_\ell)$ is given by (7). Unless otherwise specified, the numerical parameters provided in Table 1 are used in all subsequent examples.[6,7,8] The analyses are performed using a Matlab implementation of the presented framework.

Table 1 Numerical parameters used in all subsequent examples

Initial Lagrange multiplier estimators, $\lambda_j^{(1)}$	0
Initial penalty factor, $\mu^{(1)}$	10
Maximum penalty factor, $\mu_{\max}$	10,000
Penalty factor update parameter, α	1.1
SIMP penalization factor, p	3.5
Nonlinear filter exponent, q	3
Ersatz parameter, ϵ	10^{-8}
MMA iterations per AL step, `MMA_Iter`	5
MMA move limit, `move`	0.15
Initial threshold projection factor, $\bar{\beta}$[a]	1
Threshold projection factor increment, $\bar{\beta}_{inc}$[a]	1
Threshold projection factor frequency, $\bar{\beta}_{freq}$[a]	5
Maximum threshold projection factor, $\bar{\beta}_{\max}$[a]	10
Threshold projection density, $\bar{\eta}$	0.5
Initial guess, $\mathbf{z}^{(0)}$	0.5
Convergence tolerance on design variables, `Tol`	0.002
Convergence tolerance on stress constraints, `TolS`	0.003
Maximum number of AL steps, `MaxIter`	100

[a] Parameter $\bar{\beta}$ starts at 1 and increases by $\bar{\beta}_{inc}$ every $\bar{\beta}_{freq}$ AL steps and up to the maximum value, $\bar{\beta}_{\max}$

---

[6] The parameters provided in Table 1 correspond to the default parameters originally proposed by Giraldo-Londoño and Paulino (2021). We note that the parameter $\bar{\beta}_{\max}$ could be set in a manner consistent with da Silva et al. (2019) via linearization of the nonlinear filter kernel,

$$\left(1 - \frac{\|\mathbf{x}_i - \mathbf{x}_j\|_2}{R}\right)^q \approx 1 - \frac{\|\mathbf{x}_i - \mathbf{x}_j\|_2}{R/q}.$$

Using the expression, $\beta_{\text{lim}} = 2R/l_e$, from da Silva et al. (2019) and an effective filter radius of approximately R/q, one could also choose $\bar{\beta}_{\max} = 2R/ql_e$.

[7] As is the case with most topology optimization problems in the literature, the particular problem we wish to solve is nonconvex. As a consequence, gradient-based algorithms like the method employed in this work are susceptible to local minima and convergence to the global minimum cannot be guaranteed. Although we cannot avoid this fact, in the current work we attempt to make the evolution of the topology smoother by lowering the MMA `move` parameter from the default of 0.5 to 0.15 in anticipation of the nonlinearity of the optimization problem with the hope of consistently arriving at a reasonable local minimum.

[8] Although we have empirically found `MMA_Iter` = 5 to work well for most problems, should the user wish to change this parameter we note that α and $\bar{\beta}_{freq}$ should be updated according to $\alpha = 1.1^{\texttt{MMA\_Iter}/5}$ and $\bar{\beta}_{freq} = \texttt{round}(25/\texttt{MMA\_Iter}, 0)$ in order to ensure the penalty factor (μ) and threshold projection factor ($\bar{\beta}$) increase at approximately the same rate as they would with the default parameters..

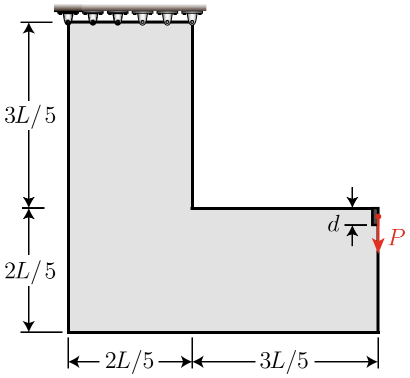

Fig. 1 L-bracket domain geometry and boundary conditions where $L = 1$ m and $d = 0.06$ m

4.1 2D L-bracket design

Results are first presented for the classical L-bracket test problem in two spatial dimensions. A finite element mesh generated using `PolyMesher` (Talischi et al. 2012a) is utilized which consists of 200,704 regular Q4 elements. The domain geometry and boundary conditions are illustrated in Fig. 1. A linear elastic material is used with Young's modulus, $E_0 = 70$ GPa, Poisson's ratio, $\nu_0 = 0.3$, and stress limit, $\sigma_{\text{lim}} = 100$ MPa. An applied load of $P = 2 \times 10^3$ kN is used and the results for various values of the weighting parameter, w, are provided in Fig. 2 with a filter radius of $R = 0.05$ m. As the weighting parameter is increased from 0 to 0.95 more emphasis is placed on reducing the compliance rather than the amount of material. This results in designs which are significantly heavier once the weighting parameter is taken sufficiently close to 1. Based on the results shown in Fig. 2, we recommend a value of $w \in [0.25, 0.5]$. Convergence plots for each of the results shown in Fig. 2 are provided in Appendix 2.

This example with a weighting parameter of $w = 0$ demonstrates two difficulties mentioned previously. In particular one can see that the compressive members in which the stress constraints are not active are still present in the design, even though they tend to be quite slender. In particular, the vertical compressive member is present in order to increase the section modulus of the structure, ultimately decreasing the tensile stress in the vertical member near the re-entrant corner. Including the compliance in the objective by increasing the weighting parameter to $w = 0.25$ or $w = 0.5$ helps to add cross-sectional area to such members which are likely quite susceptible to buckling. Additionally, the convergence plots provided in Fig. 15 of Appendix 2 highlight the stabilizing effect of introducing the compliance into the objective function. In particular, we observe smoother convergence of the maximum principal stress as w is increased (corresponding to more emphasis on reducing the compliance). Here, we also note that as w is increased, the radius of the rounded re-entrant corner is reduced in order to favor decreasing the compliance.

Additionally, Fig. 3 illustrates the effect of taking different stress limits with a fixed weighting factor of $w = 0.5$. In all presented cases the 200,704 local constraints are satisfied. Consistent with our intuition, a lower stress limit generally results in a heavier structure with thicker structural members, particularly those loaded in tension. The example with a weighting factor of $w = 0.5$ required 18 minutes running on a desktop with an Intel(R) Core(TM) i9-10900K CPU @ 3.70GHz and 64GB of RAM.

4.2 2D Notched beam design

Next, we apply the presented framework to the 2D notched beam domain with geometry and boundary conditions shown in Fig. 4. The beam is made of a linear elastic material with Young's modulus, $E_0 = 20$ GPa, Poisson's ratio, $\nu_0 = 0.3$, and stress limit, $\sigma_{\text{lim}} = 2$ MPa. A load of magnitude $P = 4 \times 10^3$ kN is distributed across a width $d = 10$ m. Subsequently, the domain is discretized into 100,000 polygonal elements and a filter radius of $R = 4$ m is chosen. Similar to the previous example, we also investigate the effect of taking different values of w on the final design, as shown by the results depicted in Fig. 5. Again we see that taking larger values of w leads to larger structural members since reducing the compliance is favored. The stress also becomes less evenly distributed as w increases since larger members lead to lower stresses except in regions near stress concentrations. This is again an effect of the compliance where the larger members are preferred for stiffness but are not required in order to satisfy the stress limit. This example required 16 minutes running on a desktop with an Intel(R) Core(TM) i9-10900K CPU @ 3.70GHz and 64GB of RAM.

4.3 2D Double L-bracket design

In this example, we consider *three* design scenarios each with up to *four* load cases and the double L-bracket geometry illustrated in Fig. 6. The domain is discretized into 306,328 regular Q4 elements and the magnitudes of the applied loads for each of the 3 design scenarios considered are also provided in Fig. 6. For the first design scenario only two load cases are considered (i.e., $F_1 = F_2 \neq 0$ and $F_3 = F_4 = 0$), whereas all four load cases are considered in the two remaining design scenarios. Note that the optimization problem extends in a straightforward manner to multiple load cases. Only the normalized compliance function (3) must be updated to include the summation over M load cases,

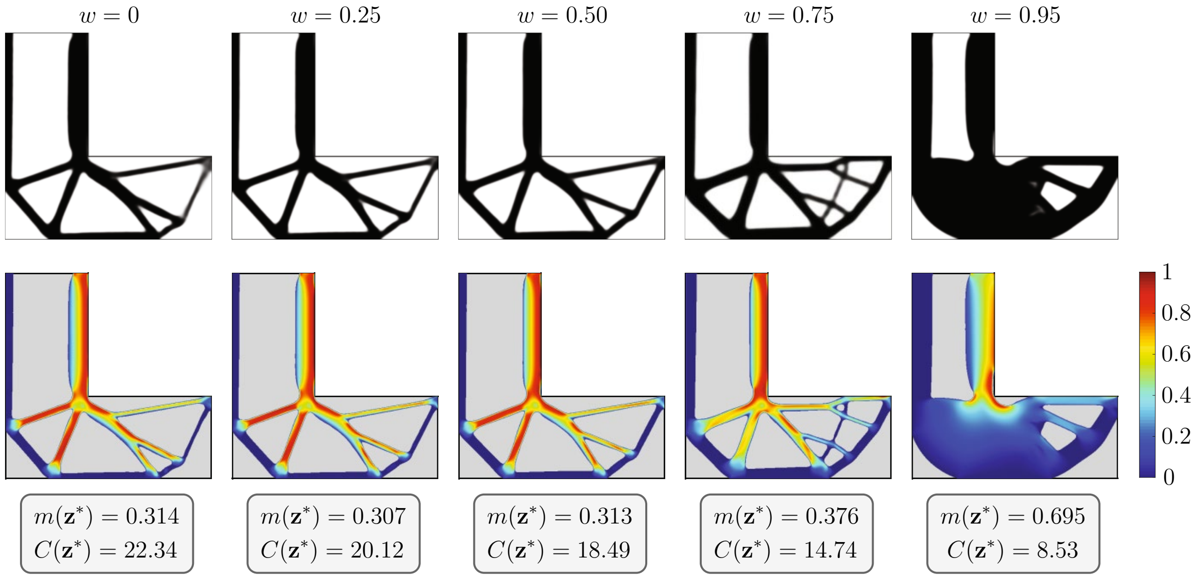

Fig. 2 L-bracket designs (top) and principal stress fields (bottom) for various values of weight factor, *w*

$$\overline{C}(\mathbf{u}^{(1)},\dots,\mathbf{u}^{(M)}) = \frac{\sum_{i=1}^{M} \mathbf{f}^{(i)^T}\mathbf{u}^{(i)}}{\sum_{i=1}^{M} \mathbf{f}^{(i)^T}\mathbf{u}_0^{(i)}} \tag{23}$$

while the additional local constraints are enforced via additional Lagrange multipliers and penalty terms as discussed in Sect. 3. Here, we consider a linear elastic material with Young's modulus, $E_0 = 70$ GPa, Poisson's ratio, $\nu_0 = 0.3$, and stress limit, $\sigma_{\lim} = 160$ MPa. A constant weighting parameter of $w = 0.5$ is used and a filter radius of $R = 0.05$ m is selected. Due to symmetry of the design domain and load cases considered in design scenarios 1 and 2, the results are also symmetric, as illustrated in Fig. 7 for these two design scenarios. For the third design scenario, however, this symmetry is broken via differing magnitudes of the vertical loads. The results for this final design scenario are also shown in Fig. 7. Note that in all cases, the local stress constraints are satisfied. Unlike the previous two examples, here we consider up to four load cases, which substantially increases the number of local stress constraints that need to be satisfied by the optimizer. For instance, design scenario 1 considers two load cases, which corresponds to 612, 656 local stress constraints, and design scenarios 2 and 3 consider four load cases, which both correspond to 1, 225, 312 local stress constraints. The example considering 2 load cases required 33 minutes, while those with 4 load cases required 62 minutes running on a desktop with an Intel(R) Core(TM) i9-10900K CPU @ 3.70GHz and 64GB of RAM.

4.4 3D corbel design

Next, results for multiple three-dimensional examples are provided, beginning with the corbel considered in this subsection. The geometry and boundary conditions are illustrated in Fig. 8. A linear elastic material is assumed with Young's modulus, $E_0 = 30$ GPa, Poisson's ratio, $\nu_0 = 0.25$, and stress limit, $\sigma_{\lim} = 5$ MPa. A traction load of $P = 0.1 \times 10^3$ kN is applied at the tip of the bracket and distributed as shown in the figure. One-half of the domain is discretized into 512,000 8-node regular hexahedral elements with symmetry boundary conditions imposed. The results obtained with two different weight factors ($w = 0.25$ and $w = 0.5$) and a filter radius of $R = 0.15$ m are provided in Fig. 9. For comparison, we also provide the results from imposing identical constraints on the von Mises stress measure (omitting the principal stress constraints) with otherwise identical numerical parameters. Here we note the design asymmetry induced via the tension/compression loading asymmetry of the boundary value problem when the maximum principal stress is constrained. This is similar but not equivalent to the effect of the Drucker-Prager criterion (among others) for which a similar topology might be obtained, such as the one presented in Fig. 5 by Giraldo-Londoño and Paulino (2020), for example. In contrast, von Mises stress constraints result in a perfectly symmetric structure, which is also the case for the Tresca criterion as shown in the aforementioned work. Furthermore, the stress singularity is not removed in the compression-dominated part of the domain when principal stress constraints are imposed, with the opposite behavior observed when constraining the von Mises stress measure.

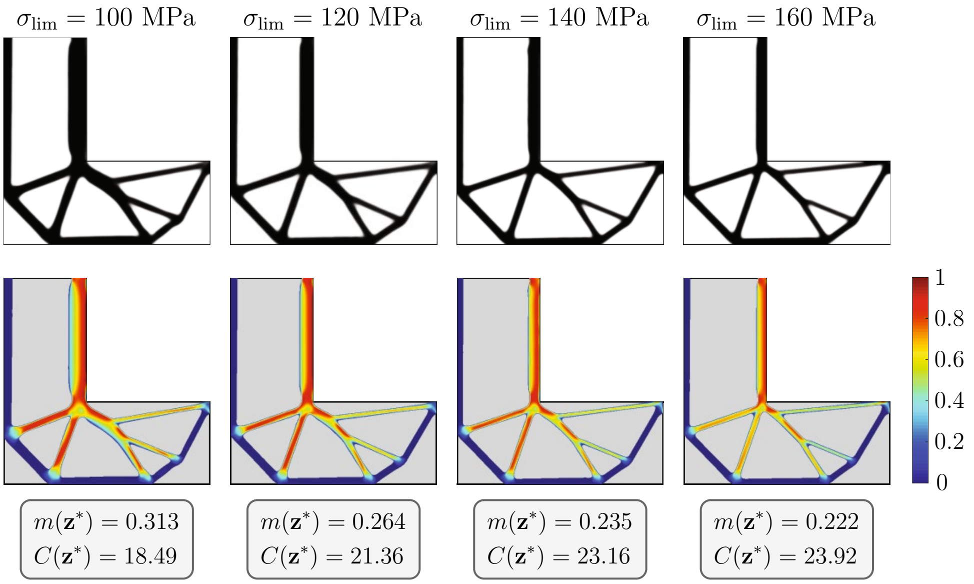

Fig. 3 L-bracket designs (top) and principal stress fields (bottom) for various values of stress limit, σ_{lim}

The different weight factors produce minor changes in the final topologies, which result in intuitive trade-offs between the final volume fraction and compliance of each structure. In the case of the principal stress-constrained design, increasing the weight factor from $w = 0.25$ to $w = 0.5$ resulted in 32.5% lower compliance at the cost of 7.5% additional material. For the von Mises stress measure, the increased weight factor produced 12% lower compliance but required 11% more material. Interestingly, the percent decrease in compliance is very large compared to the required percent increase in material when the maximum principal stress is constrained. In contrast, a mild percent decrease in compliance and a larger percent increase in material is observed when using the von Mises stress measure. This is likely a result of fewer active constraints when the principal stress measure is employed and, consequently, a larger feasible design space. Finally, we note the generally lower stresses produced throughout each structure when the weight factor is increased, due primarily to the additional material required to increase the stiffness. The von Mises and maximum principal stress examples required 6 and 8 h, respectively, running on a cluster with an Intel(R) Xeon(R) Gold 6226R CPU, NVIDIA A100 GPU, and 320GB of RAM.

4.5 3D bridge design

Next, we present the results for the three-dimensional bridge domain with geometry and boundary conditions[9] illustrated in Fig. 10. The bridge is made of a linear elastic material with Young's modulus, $E_0 = 20$ GPa, Poisson's ratio, $\nu_0 = 0.25$, and stress limit, $\sigma_{\mathrm{lim}} = 4$ MPa. A distributed load of magnitude $P = 80 \times 10^3$ kN is applied to the deck surface. Two separate finite element meshes are created for one-quarter of the domain with symmetry boundary conditions imposed. The coarser mesh consists of 115,800 regular 8-node hexahedral elements, whereas the finer mesh contains 393,750 elements. Results are obtained using a weighting parameter of $w = 0.25$ and a filter radius of $R = 1.5$ m.

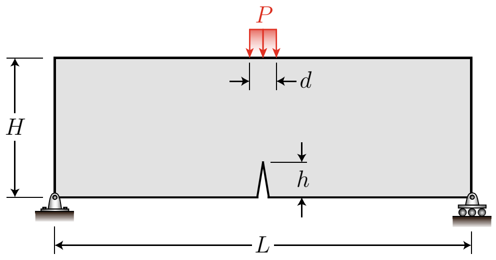

Fig. 4 Notched beam geometry and boundary conditions. $L = 360$ m, $H = 120$ m, $h = 30$ m, $d = 10$ m

---

[9] Note that our boundary conditions are different from those presented in the 2D bridge example of Amstutz et al. (2012). In the aforementioned work, the boundary conditions permit the formation of a compression arch whereas those in our example do not afford such a possibility.

Fig. 5 Notched beam designs (left) and principal stress fields (right) obtained with different values of the weighting parameter, *w*

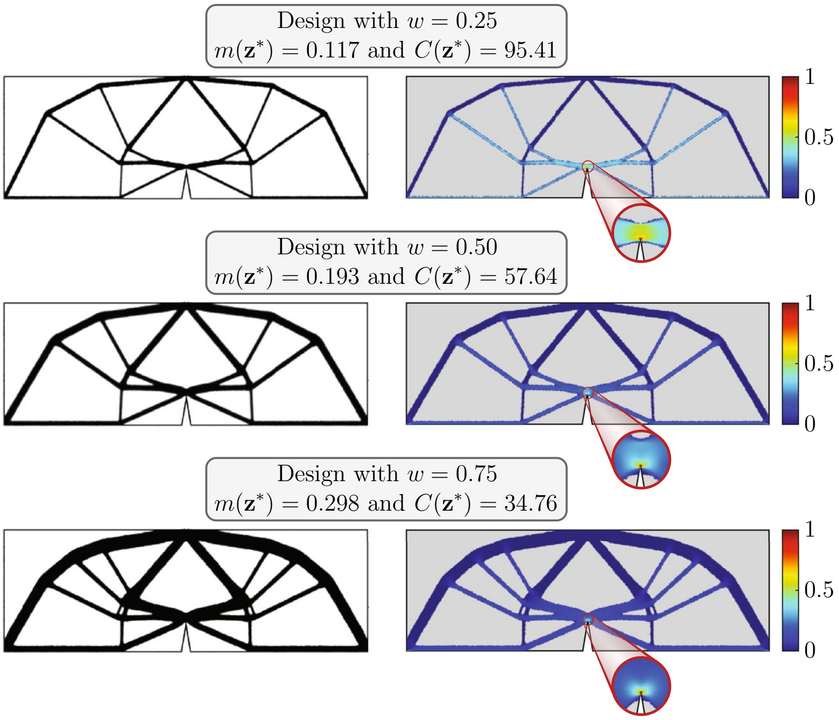

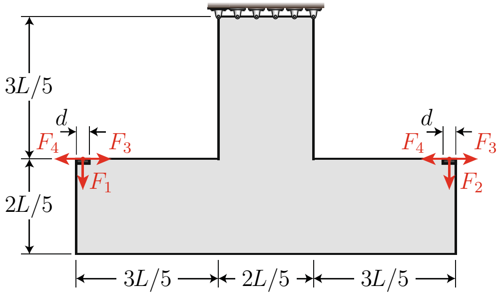

	F_1 ($\times 10^3$ kN)	F_2 ($\times 10^3$ kN)	F_3 ($\times 10^3$ kN)	F_4 ($\times 10^3$ kN)
Design 1	2	2	–	–
Design 2	2	2	1	1
Design 3	3	2	1	1

Fig. 6 Double L-bracket domain geometry ($L = 1$ m and $d = 0.06$ m) and loads corresponding to each design scenario

The resulting topology and stresses are shown in Figs. 11 and 12 for the coarse and fine mesh, respectively. While the two different mesh sizes result in slightly different numbers of structural members, the resulting volume fraction and compliance values are nearly identical. More importantly, the maximum principal stresses are all within the specified limit throughout each domain with identical input parameters, despite the fact that the finer mesh required enforcement of 340% more local constraints. Additionally, the finer mesh results in more supporting members for the bottom of the deck when compared with the coarse mesh results, due primarily to the additional design freedom. In both cases, the bottom chord is loaded in tension and is almost entirely near the specified stress limit. This is in contrast to the struts supporting the deck which are clearly in compression, resulting in no active constraints in that region. This numerical example required 27 minutes (coarse mesh) and 3 h (fine mesh) of compute time running on a cluster with an Intel(R) Xeon(R) Gold 6226R CPU, NVIDIA A100 GPU, and 320GB of RAM.

4.6 Benchmarking: 3D antenna support bracket design

Finally, we propose a 3D antenna support bracket design as a benchmark problem for the field of stress-constrained topology optimization. Here, we investigate this realistic engineering design problem with domain and boundary conditions briefly illustrated in Fig. 13. Note the presence of multiple passive regions of elements which are not designed. Due to the complexity of the geometry, we provide an IGES CAD file in the Electronic Supplemental Information. Design

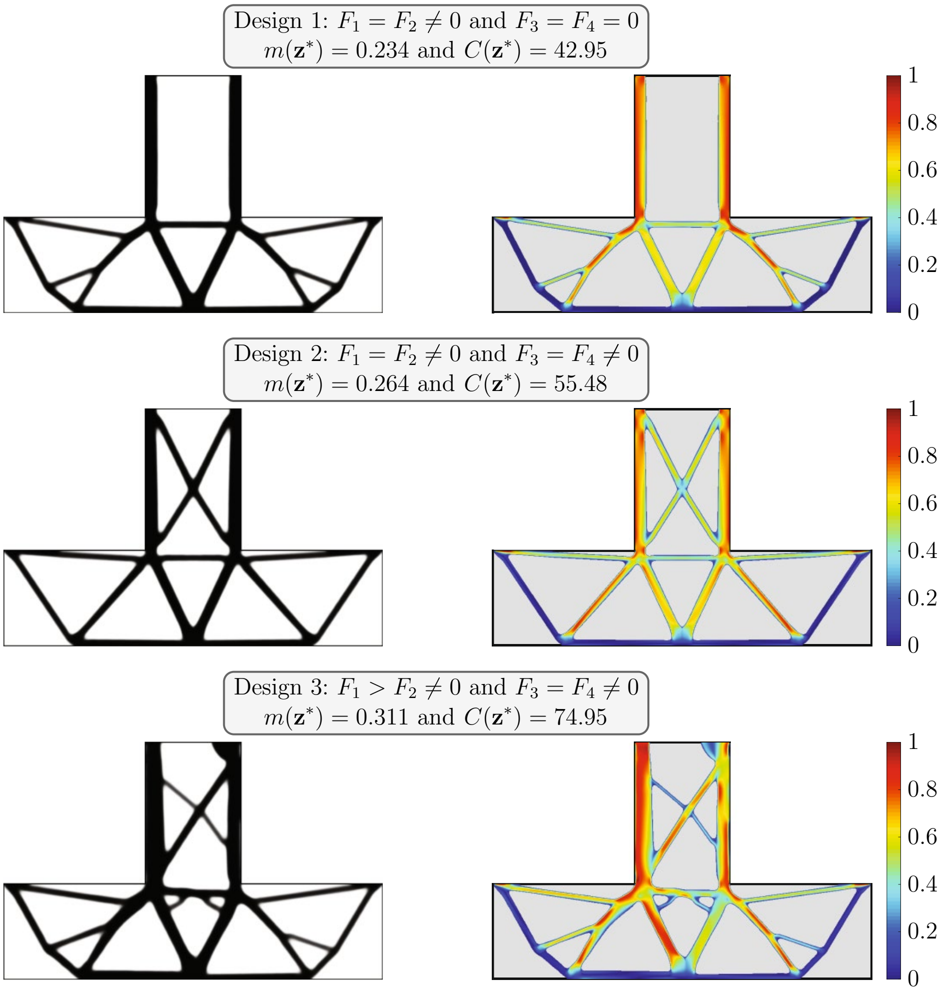

Fig. 7 Final designs (left) and principal stress fields (right)

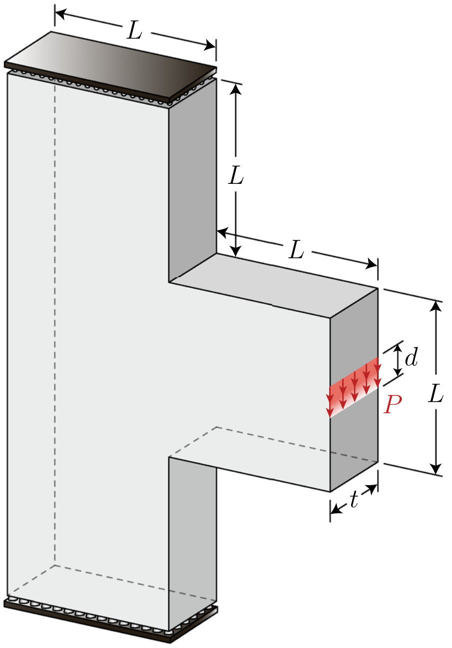

Fig. 8 Corbel domain and boundary conditions where $L = 2$ m and $d = 0.4$ m

symmetry is enforced using a symmetry filter applied about the x-z plane (Giraldo-Londoño and Paulino 2021). The bracket is assumed to be made of a linear elastic material with Young's modulus, $E_0 = 70$ GPa, Poisson's ratio, $\nu_0 = 0.33$, and stress limit, $\sigma_{\text{lim}} = 140$ MPa. Traction loads are evenly applied to the bolt holes depicted in Fig. 13b, such that the total magnitude of the load in the x direction equals 1×10^3 kN, and that in the y and z directions each equals 0.05×10^3 kN. We obtain numerical results using a weight factor of $w = 0.25$, along with a filter radius of $R = 0.03$ m. The domain is discretized into an unstructured mesh of 1,190,344 8-node hexahedral elements, corresponding to 1,190,344 local stress constraints which must be enforced. The resulting topology and stresses are shown in Fig. 14. For comparison, the results without stress constraints are also provided. It is interesting to note that in the compression-dominated region (shown in the top row of Fig. 14) the designs with and without stress constraints are nearly identical, whereas the region loaded in tension is substantially modified. The stresses exceed the limit in multiple parts of the domain when the stress constraints are omitted, and one

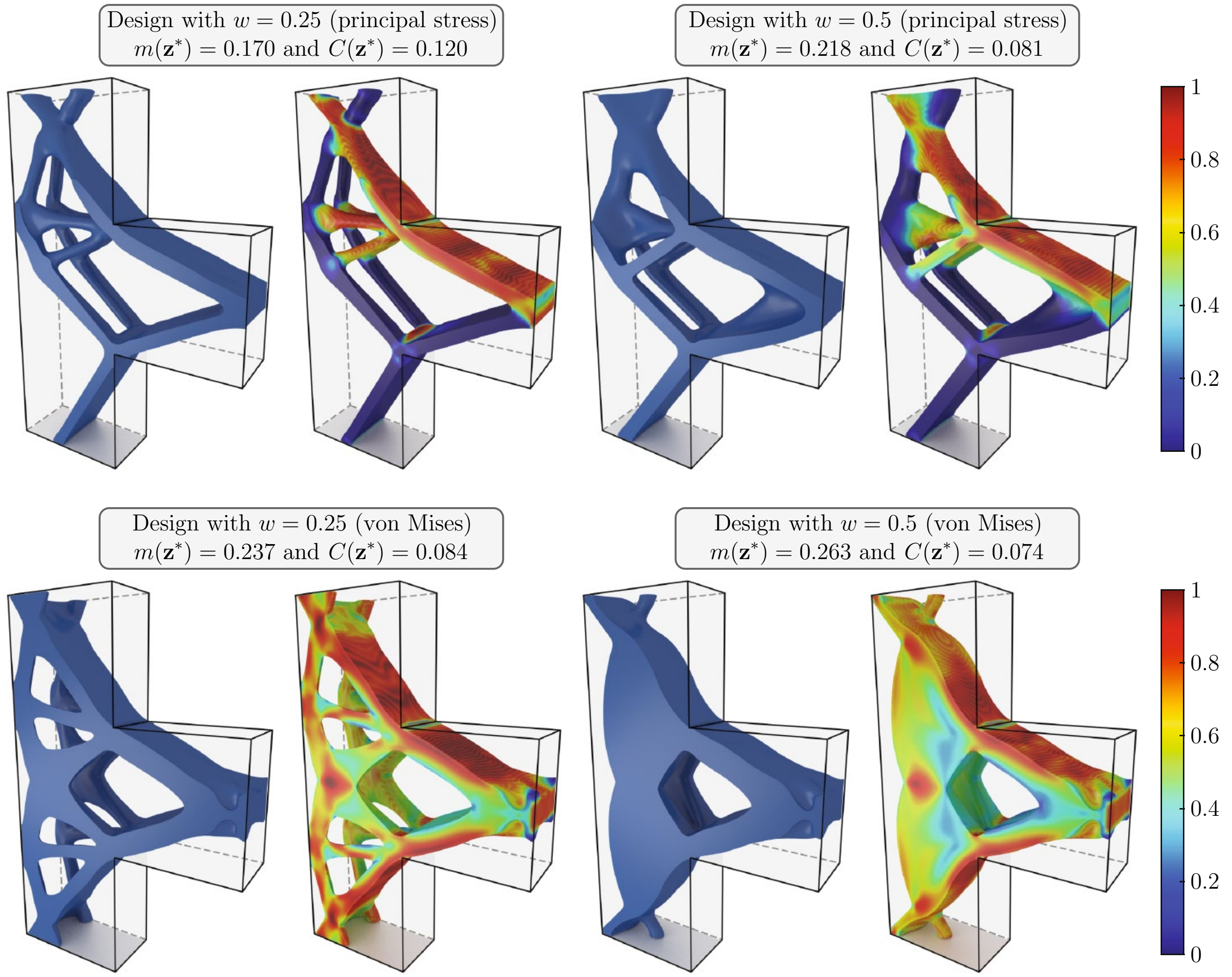

Fig. 9 Corbel design and principal stress fields considering the principal stress constraints (top) and von Mises stress constraints (bottom). For each type of stress constraint, two values of w are chosen to evaluate its effect in the optimized topology of a 3D problem. The results displayed here were obtained after discretizing one-half of the domain using 512,000 regular hexahedral elements

such region is highlighted in the same figure. Furthermore, while the stress-constrained design does not suffer from significantly higher volume fraction ($\approx 0.9\%$ more material required) the compliance is roughly 13.4% larger, indicating that the optimizer has sacrificed stiffness rather than mass in order to ensure the stresses are below the specified limit. This numerical example required approximately 9 h of compute time running on a cluster with an Intel(R) Xeon(R) Gold 6226R CPU, NVIDIA A100 GPU, and 320GB of RAM.

5 Concluding remarks

A tailored topology optimization formulation was presented for structural design limiting the maximum principal stress using an augmented Lagrangian framework. While the vast majority of the topology optimization literature has focused on von Mises based stress-constrained design, there are a large class of materials (e.g., brittle materials) in which the maximum principal stress is a more appropriate stress measure to limit. The augmented Lagrangian method enables the imposition of the local constraints without the need for artifacts, such as aggregation schemes and/or clustering methods, which are neither consistent with the local nature of stress nor robust numerically as they require the selection of parameters that must often be modified depending on the specific problem under consideration. Analytical sensitivities of the relevant functions are derived, which facilitate the efficient solution of the optimization problem with gradient-based algorithms. The addition of the compliance to the aggregate objective function serves multiple purposes including stabilizing the evolution of the topology and preventing unreasonably thin, compressive members which may ultimately be susceptible to buckling. One important

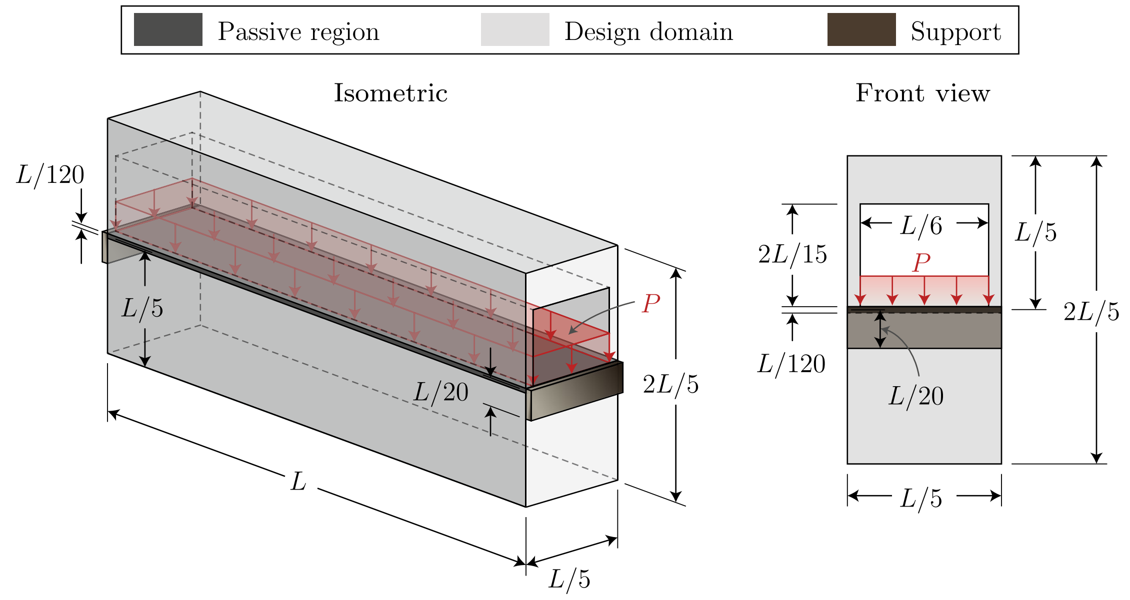

Fig. 10 Bridge domain and boundary conditions, $L = 60$ m

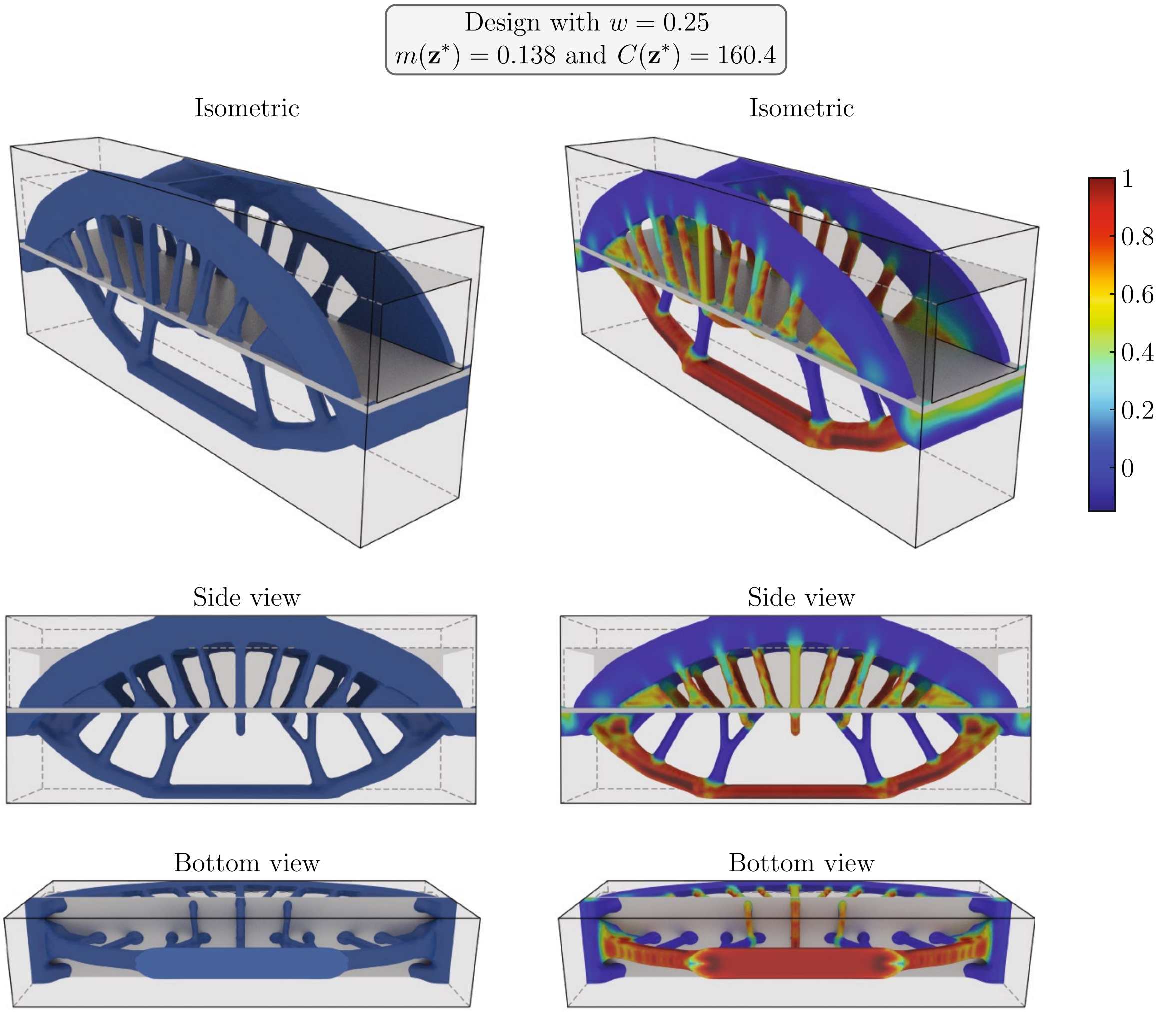

Fig. 11 Bridge design (left) and principal stress fields (right). The results displayed here are obtained after discretizing one-quarter of the domain using 115,800 regular hexahedral elements

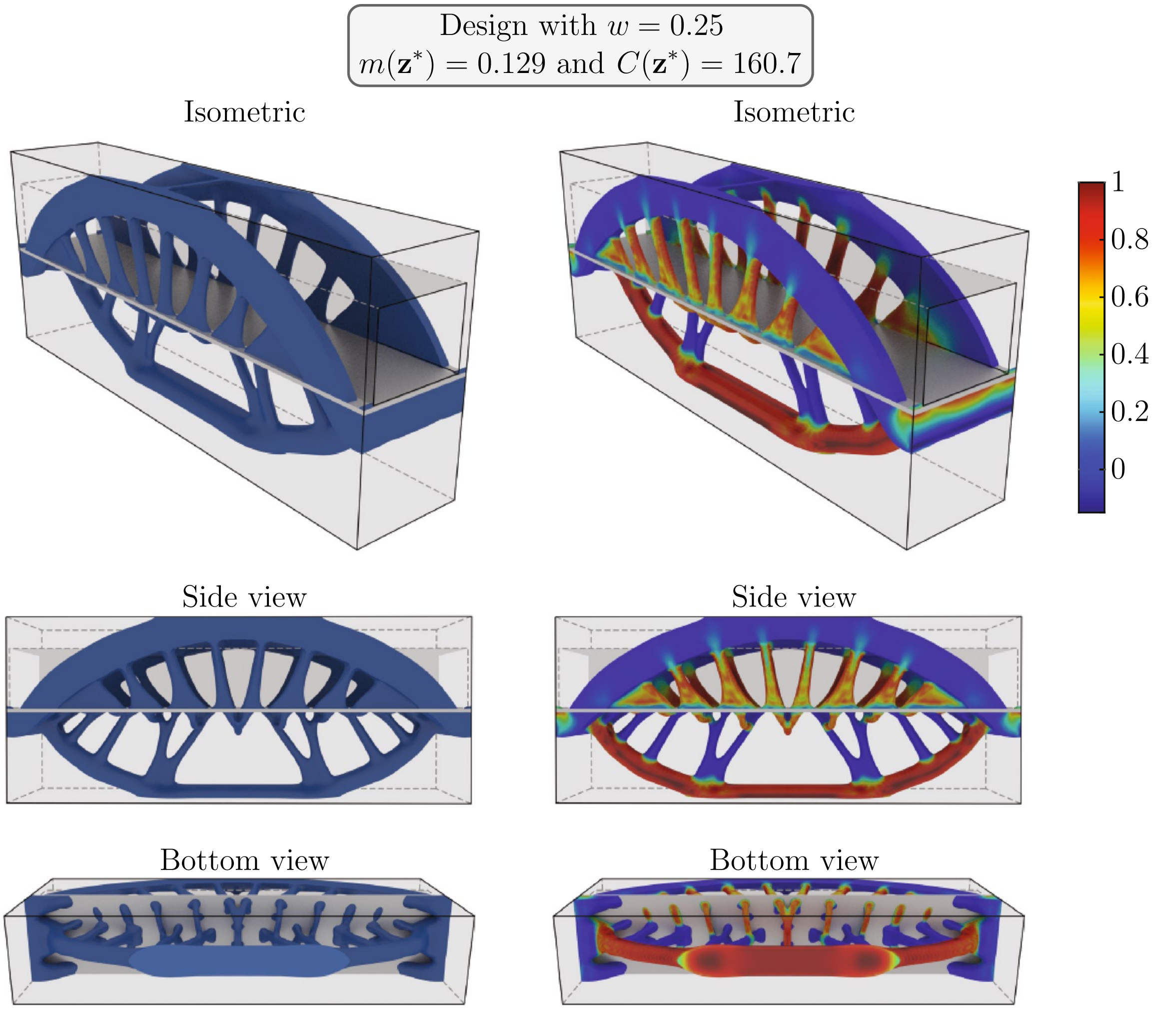

Fig. 12 Bridge design (left) and principal stress fields (right). The results displayed here are obtained after discretizing one-quarter of the domain using 393,750 regular hexahedral elements

potential path for future improvement of the presented formulation would be to incorporate buckling constraints directly in the optimization problem definition as an alternative to the compliance in order to provide additional support for compression-dominated regions.

It is demonstrated, through numerous two- and three-dimensional examples, that this framework is not only effective for small-scale design, but can also handle problems in which millions of local constraints must be simultaneously imposed. This property renders the formulation significantly more useful in practice, where complex geometries must often be approximated with relatively large finite element discretizations. To this effect, we have proposed a benchmark problem, consisting of a three-dimensional antenna bracket design, which can be used to evaluate the performance of other formulations for stress-constrained topology optimization (due to the complexity of the geometry, the IGES CAD file is provided as electronic supplementary information). Thus, we hope that other algorithms for stress constraints can be tested against this benchmark.

Appendix 1: Sensitivity analysis

The sensitivity of the AL function in (19) is written as

$$\frac{\partial J^{(k)}}{\partial z_e} = \sum_{\ell=1}^{N} \left(\frac{\partial E_\ell}{\partial z_e} \frac{\partial J^{(k)}}{\partial E_\ell} + \frac{\partial V_\ell}{\partial z_e} \frac{\partial J^{(k)}}{\partial V_\ell} \right) \tag{24}$$

or in vector form as

$$\frac{\partial J^{(k)}}{\partial \mathbf{z}} = \frac{\partial \mathbf{E}}{\partial \mathbf{z}} \frac{\partial J^{(k)}}{\partial \mathbf{E}} + \frac{\partial \mathbf{V}}{\partial \mathbf{z}} \frac{\partial J^{(k)}}{\partial \mathbf{V}}, \tag{25}$$

where $\mathbf{E} = \{E_\ell\}_{\ell=1}^N$, $\mathbf{V} = \{V_\ell\}_{\ell=1}^N$,

$$\frac{\partial \mathbf{E}}{\partial \mathbf{z}} = \mathbf{P}^T J_{m_E}(\mathbf{Pz}) \text{ and } \frac{\partial \mathbf{V}}{\partial \mathbf{z}} = \mathbf{P}^T J_{m_V}(\mathbf{Pz}) \tag{26}$$

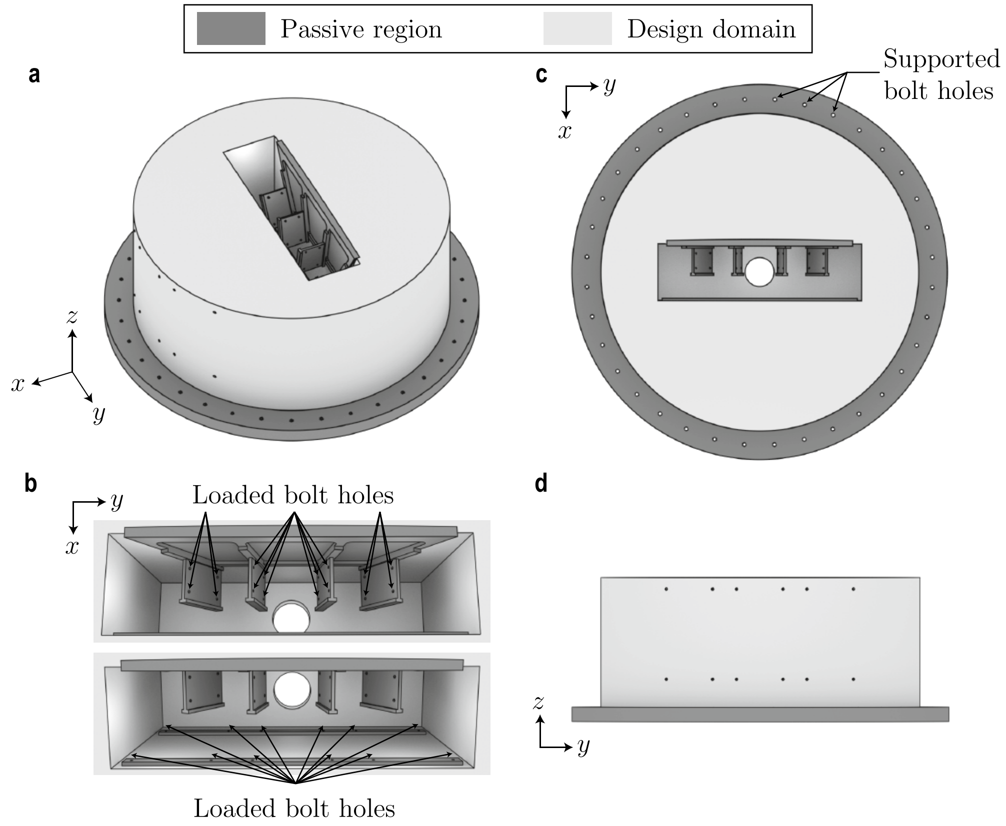

Fig. 13 Antenna support bracket domain

and $J_{m_E} = \mathrm{diag}(m'_E(y_1), \dots, m'_E(y_N))$ and $J_{m_V} = \mathrm{diag}(m'_V(y_1), \dots, m'_V(y_N))$ (Talischi et al. 2012b). Based on the functional form of the AL function in (19), we rewrite (25) as follows:

$$\frac{\partial J^{(k)}}{\partial \mathbf{z}} = \frac{\partial \mathbf{E}}{\partial \mathbf{z}}\left(\frac{\partial f}{\partial \mathbf{E}} + \frac{1}{N}\frac{\partial P^{(k)}}{\partial \mathbf{E}}\right) + \frac{\partial \mathbf{V}}{\partial \mathbf{z}}\left(\frac{\partial f}{\partial \mathbf{V}} + \frac{1}{N}\frac{\partial P^{(k)}}{\partial \mathbf{V}}\right), \tag{27}$$

where

$$P^{(k)} = \sum_{j=1}^{N}\left[\lambda_j^{(k)} h_j(\mathbf{z},\mathbf{u}) + \frac{\mu^{(k)}}{2} h_j(\mathbf{z},\mathbf{u})^2\right], \tag{28}$$

Recalling that $h_j(\mathbf{z},\mathbf{u}) = \max[g_j(\mathbf{z},\mathbf{u}), -\lambda_j^{(k)}/\mu^{(k)}]$ and $g_j(\mathbf{z},\mathbf{u}) = E_j\Lambda_j(\Lambda_j^2 + 1)$, we obtain

$$\frac{\partial P^{(k)}}{\partial V_\ell} = 0 \tag{29}$$

and

$$\frac{\partial P^{(k)}}{\partial E_\ell} = \sum_{j=1}^{N}\left[\lambda_j^{(k)} + \mu^{(k)} h_j(\mathbf{z},\mathbf{u})\right]\left[\frac{\partial h_j(\mathbf{z},\mathbf{u})}{\partial E_\ell} + \frac{\partial h_j(\mathbf{z},\mathbf{u})}{\partial \mathbf{u}} \cdot \frac{\partial \mathbf{u}}{\partial E_\ell}\right]. \tag{30}$$

Using a standard adjoint sensitivity analysis procedure, we add the sensitivity of the equilibrium equation, $\mathbf{Ku} = \mathbf{f}$, to (30) to avoid the expensive computation of $\partial \mathbf{u}/\partial E_\ell$. By doing so, we obtain

$$\frac{\partial P^{(k)}}{\partial E_\ell} = \sum_{j=1}^{N}\left[\lambda_j^{(k)} + \mu^{(k)} h_j(\mathbf{z},\mathbf{u})\right]\left[\frac{\partial h_j(\mathbf{z},\mathbf{u})}{\partial E_\ell} + \frac{\partial h_j(\mathbf{z},\mathbf{u})}{\partial \mathbf{u}} \cdot \frac{\partial \mathbf{u}}{\partial E_\ell}\right] + \xi^T\left(\mathbf{K}\frac{\partial \mathbf{u}}{\partial E_\ell} + \frac{\partial \mathbf{K}}{\partial E_\ell}\mathbf{u}\right) \tag{31}$$

We collect all the terms in (31) that multiply $\partial \mathbf{u}/\partial E_\ell$ and choose the adjoint variable ξ such that these terms vanish. After doing that, we obtain the following:

$$\frac{\partial P^{(k)}}{\partial E_\ell} = \sum_{j=1}^{N}\left[\lambda_j^{(k)} + \mu^{(k)} h_j(\mathbf{z},\mathbf{u})\right]\frac{\partial h_j(\mathbf{z},\mathbf{u})}{\partial E_\ell} + \xi^T\frac{\partial \mathbf{K}}{\partial E_\ell}\mathbf{u}, \tag{32}$$

where ξ solves the adjoint problem:

$$\mathbf{K}\xi = -\sum_{j=1}^{N}\left[\lambda_j^{(k)} + \mu^{(k)} h_j(\mathbf{z},\mathbf{u})\right]\frac{\partial h_j(\mathbf{z},\mathbf{u})}{\partial \mathbf{u}}. \tag{33}$$

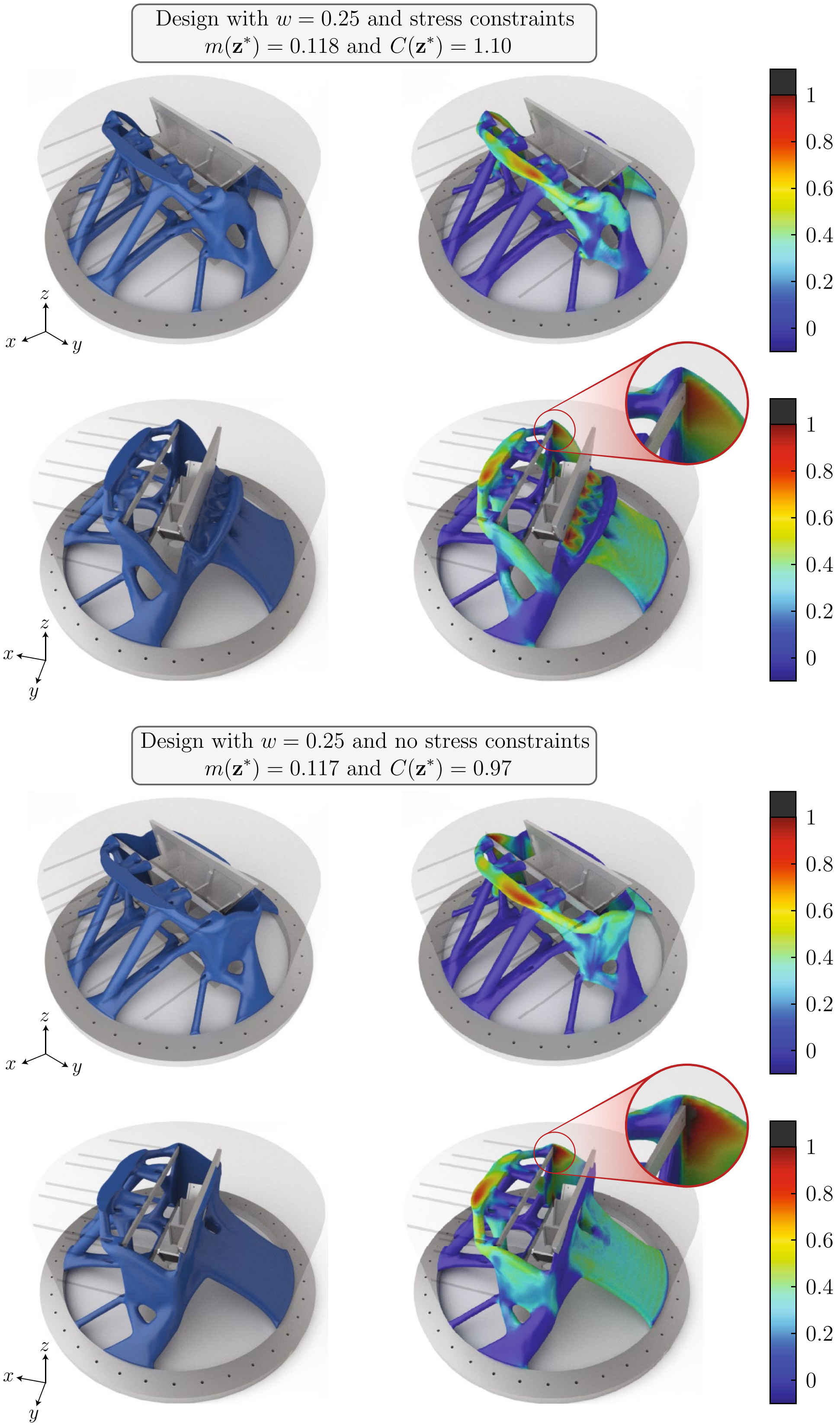

Design with $w = 0.25$ and stress constraints
$m(\mathbf{z}^*) = 0.118$ and $C(\mathbf{z}^*) = 1.10$

Design with $w = 0.25$ and no stress constraints
$m(\mathbf{z}^*) = 0.117$ and $C(\mathbf{z}^*) = 0.97$

Fig. 14 Antenna support bracket design and principal stress fields when including stress constraints (top) and omitting stress constraints (bottom). Both problems were performed using the same 1,190,344 element mesh

We use (6) to compute the term $(\partial \mathbf{K}/\partial E_\ell)\mathbf{u}$ in (32) in an element-wise fashion as

$$\frac{\partial \mathbf{K}}{\partial E_\ell}\mathbf{u} = \mathbf{k}_\ell \mathbf{u}_\ell, \tag{34}$$

where $\mathbf{u}_\ell$ is the displacement vector of element ℓ. To obtain $\partial P^{(k)}/\partial E_\ell$ using (32)–(33), we need to compute $\partial h_j/\partial E_\ell$ and $\partial h_j/\partial \mathbf{u}$. To obtain the former, we use (8) and (20), which yields

$$\frac{\partial h_j(\mathbf{z},\mathbf{u})}{\partial E_\ell} = \begin{cases} \Lambda_j(\Lambda_j^2+1)\delta_{\ell j} & \text{when } g_j(\mathbf{z},\mathbf{u}) < -\lambda_j^{(k)}/\mu^{(k)} \\ 0 & \text{otherwise,} \end{cases} \tag{35}$$

where $\delta_{\ell j}$ is the Kronecker delta operator. Using the chain rule, we obtain

$$\begin{aligned} \frac{\partial h_j}{\partial \mathbf{u}} &= \frac{\partial g_j}{\partial \mathbf{u}} \\ &= \frac{\partial g_j}{\partial \Lambda_j}\left(\frac{\partial \Lambda_j}{\partial I_1}\frac{\partial I_1}{\partial \boldsymbol{\sigma}} + \frac{\partial \Lambda_j}{\partial J_2}\frac{\partial J_2}{\partial \boldsymbol{\sigma}} + \frac{\partial \Lambda_j}{\partial J_3}\frac{\partial J_3}{\partial \boldsymbol{\sigma}}\right)\cdot\frac{\partial \boldsymbol{\sigma}}{\partial \mathbf{u}} \end{aligned} \tag{36}$$

when $g_j(\mathbf{z},\mathbf{u}) < -\lambda_j^{(k)}/\mu^{(k)}$ and $\frac{\partial h_j(\mathbf{z},\mathbf{u})}{\partial E_\ell} = 0$ otherwise. For the sake of completeness, below we provide all partial derivatives needed to evaluate $\partial h_j/\partial \mathbf{u}$.Using (8), we obtain

$$\frac{\partial g_j}{\partial \Lambda_j} = E_j(3\Lambda_j^2+1). \tag{37}$$

From (9), (10), (17), and (18), we obtain

$$\begin{aligned} \frac{\partial \Lambda_j}{\partial I_1} &= \frac{1}{\sigma_{\lim}}\left[\frac{2}{\sqrt{3}}\sqrt{J_2}\cos(\theta+2\pi/3)\frac{\partial \theta}{\partial J_3}\frac{\partial J_3}{\partial I_1} + \frac{1}{3}\right], \\ \frac{\partial \Lambda_j}{\partial J_2} &= \frac{1}{\sigma_{\lim}}\left[\frac{2}{\sqrt{3}}\sqrt{J_2}\cos(\theta+2\pi/3)\left(\frac{\partial \theta}{\partial J_2} + \frac{\partial \theta}{\partial J_3}\frac{\partial J_3}{\partial J_2}\right) + \frac{1}{\sqrt{3J_2}}\sin(\theta+2\pi/3)\right], \quad \text{and} \\ \frac{\partial \Lambda_j}{\partial J_3} &= 0 \end{aligned} \tag{38}$$

for 2D problems, and

$$\begin{aligned} \frac{\partial \Lambda_j}{\partial I_1} &= \frac{1}{3\sigma_{\lim}}, \\ \frac{\partial \Lambda_j}{\partial J_2} &= \frac{1}{\sigma_{\lim}}\left[\frac{2}{\sqrt{3}}\sqrt{J_2}\cos(\theta+2\pi/3)\frac{\partial \theta}{\partial J_2} + \frac{1}{\sqrt{3J_2}}\sin(\theta+2\pi/3)\right], \quad \text{and} \\ \frac{\partial \Lambda_j}{\partial J_3} &= \frac{1}{\sigma_{\lim}}\left[\frac{2}{\sqrt{3}}\sqrt{J_2}\cos(\theta+2\pi/3)\frac{\partial \theta}{\partial J_3}\right] \end{aligned} \tag{39}$$

for 3D problems. The partial derivatives, $\partial\theta/\partial J_2$ and $\partial\theta/\partial J_3$, are obtained from direct differentiation of (11), and $\partial J_3/\partial I_1$ and $\partial J_3/\partial J_2$ are obtained from (17). In addition, from (14), (15), (17), and (18), we obtain

$$\frac{\partial I_1}{\partial \boldsymbol{\sigma}} = \overline{\mathbf{M}}^T, \tag{40}$$

$$\frac{\partial J_2}{\partial \boldsymbol{\sigma}} = \frac{2}{3}\overline{\mathbf{V}}\boldsymbol{\sigma}, \tag{41}$$

and[10]

$$\frac{\partial J_3}{\partial \boldsymbol{\sigma}} = \begin{bmatrix} s_{22}s_{33} - \sigma_{23}^2 \\ s_{11}s_{33} - \sigma_{13}^2 \\ s_{11}s_{22} - \sigma_{12}^2 \\ 2(\sigma_{13}\sigma_{12} - s_{11}\sigma_{23}) \\ 2(\sigma_{12}\sigma_{23} - s_{22}\sigma_{13}) \\ 2(\sigma_{23}\sigma_{13} - s_{33}\sigma_{12}) \end{bmatrix} + \frac{J_2}{3}\begin{bmatrix} 1 \\ 1 \\ 1 \\ 0 \\ 0 \\ 0 \end{bmatrix}. \tag{42}$$

Finally, the sensitivity of the Cauchy stress with respect to the displacement vector is obtained as

$$\frac{\partial \boldsymbol{\sigma}}{\partial \mathbf{u}} = \frac{\partial \boldsymbol{\sigma}}{\partial \boldsymbol{\varepsilon}}\cdot\frac{\partial \boldsymbol{\varepsilon}}{\partial \mathbf{u}} = \mathbf{DB} \tag{43}$$

Appendix 2: Convergence plots for selected problems

Convergence plots for the L-bracket, notched beam, and double L-bracket examples are shown in Figs. 15, 16, and 17, respectively.

---

[10] Note that $\partial J_3/\partial \boldsymbol{\sigma}$ is only needed for 3D problems.

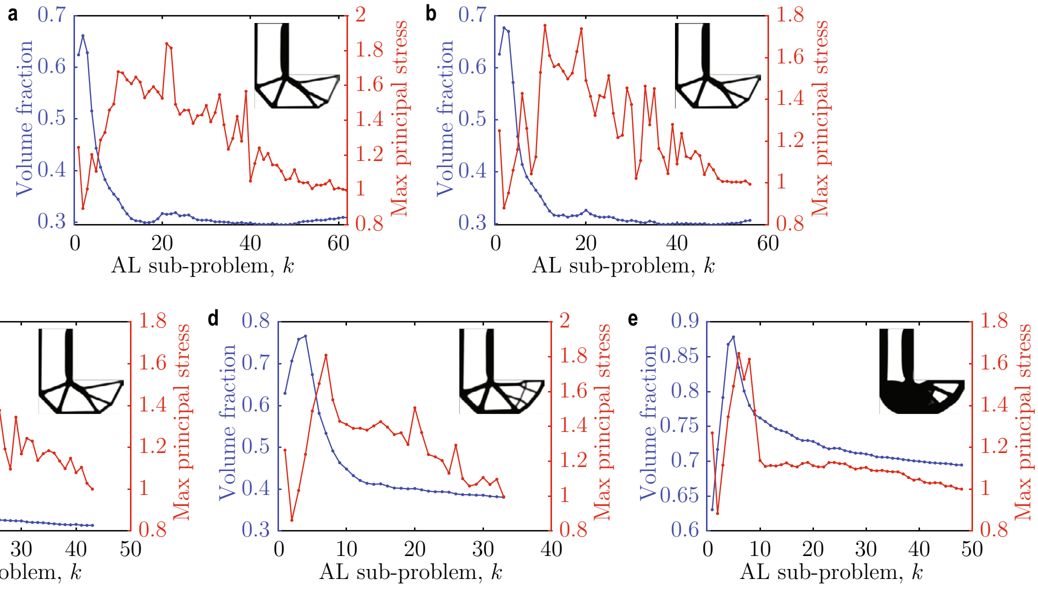

Fig. 15 Convergence plots for the L-bracket example

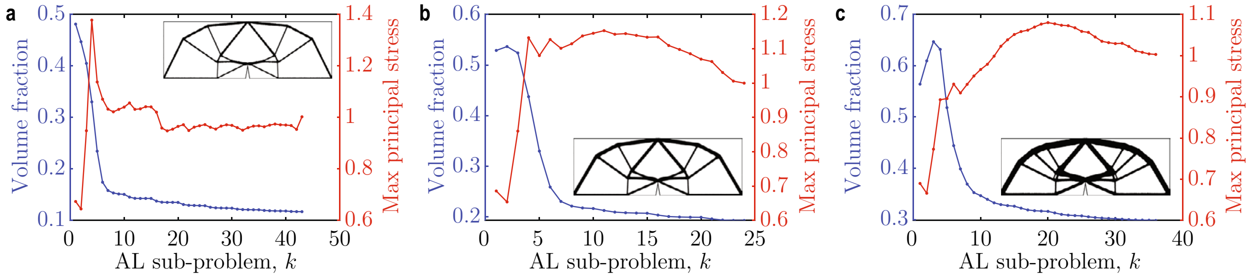

Fig. 16 Convergence plots for the notched beam example

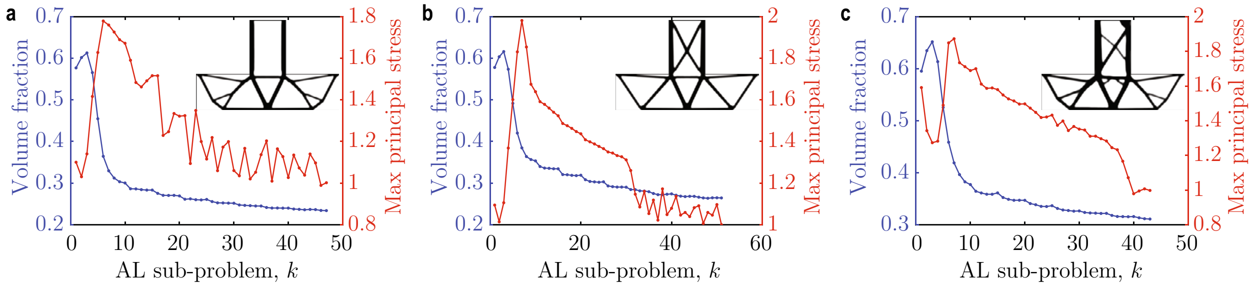

Fig. 17 Convergence plots for the double L-bracket example

Appendix 3: 2D bridge design subject to tensile/compressive stress constraints

In this example, we apply the presented framework to design a 2D bridge subjected to constraints on both maximum principal stresses (tensile stresses) and minimum principal stresses (compressive stresses). In order to also enforce a compressive stress limit, $\sigma^c_{\text{lim}} > 0$, on the minimum principal

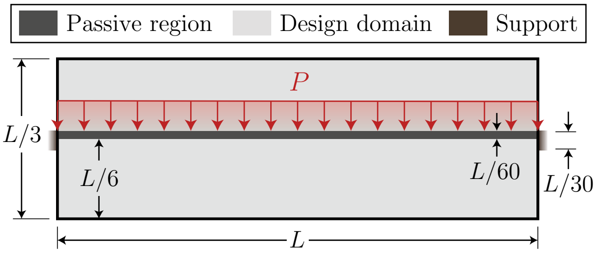

Fig. 18 2D bridge geometry and boundary conditions, $L = 180$ m

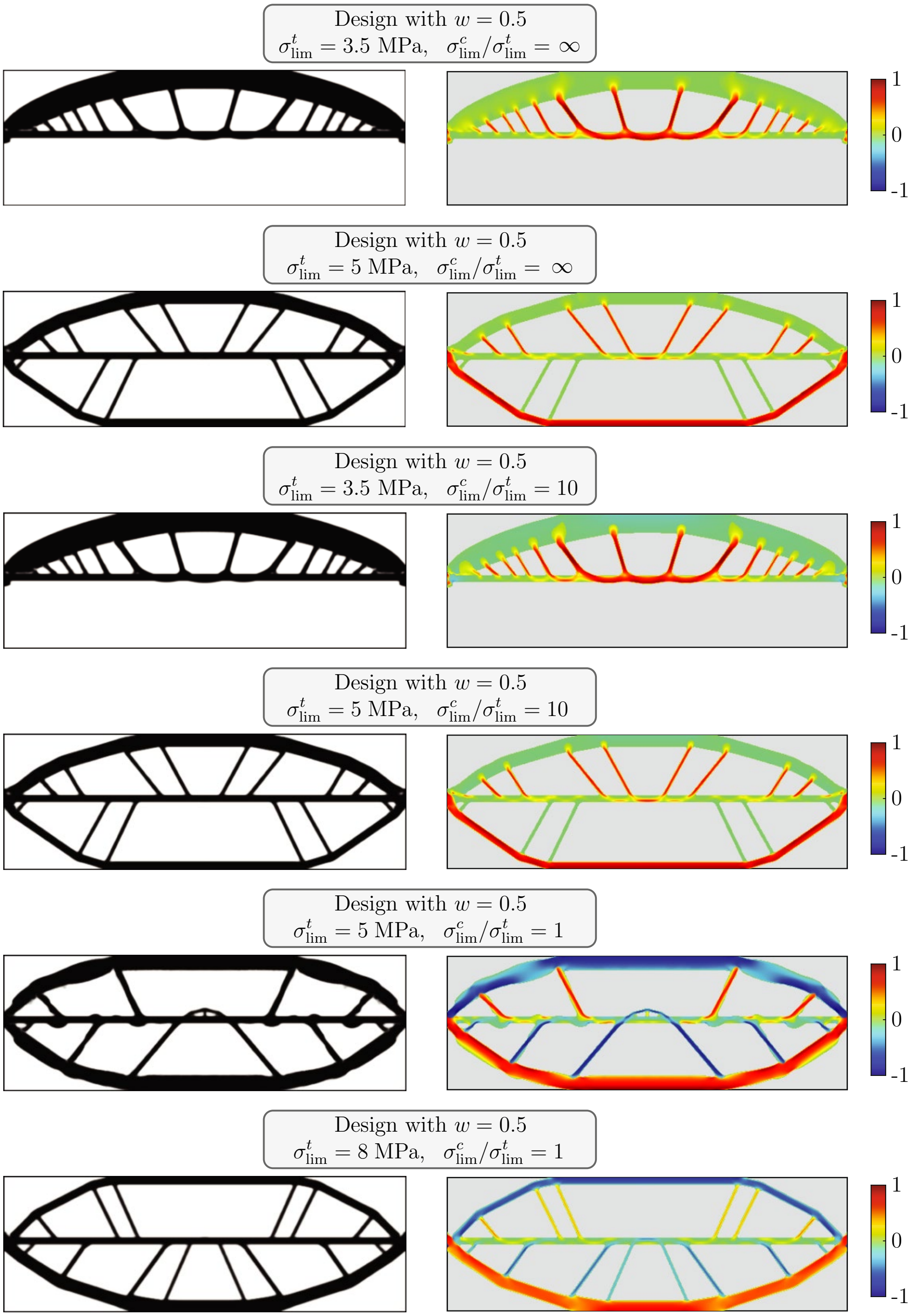

Fig. 19 2D bridge designs (left) and largest principal stress fields (right) for various tensile stress limits, $\sigma^t_{\lim}$ and compressive-to-tensile stress limit ratio, $\sigma^c_{\lim}/\sigma^t_{\lim}$. The largest principal stress ratio in magnitude is illustrated with the correct sign via the expression $\max\left(|\widetilde{\sigma}^1_\ell|, |\widetilde{\sigma}^3_\ell|\right) \cdot \operatorname{sign}(\widetilde{\sigma}^1_\ell + \widetilde{\sigma}^3_\ell)$, where $\widetilde{\sigma}^1_\ell = E_\ell \sigma^1_\ell / \sigma^t_{\lim}$ and $\widetilde{\sigma}^3_\ell = E_\ell \sigma^3_\ell / \sigma^c_{\lim}$

stress, σ_3, the additional constraints are augmented in a similar manner to the maximum principal stress constraints in which Eq. (9) is replaced with $\Lambda_j = -\sigma^3_j/\sigma^c_{\lim} - 1$, corresponding to a lower bound. The domain geometry and boundary conditions are shown in Fig. 18. The bridge is loaded with a uniformly distributed load of magnitude $P = 5 \times 10^3$ kN applied over the surface of the deck. Moreover, the domain is discretized using 97,200 regular Q4

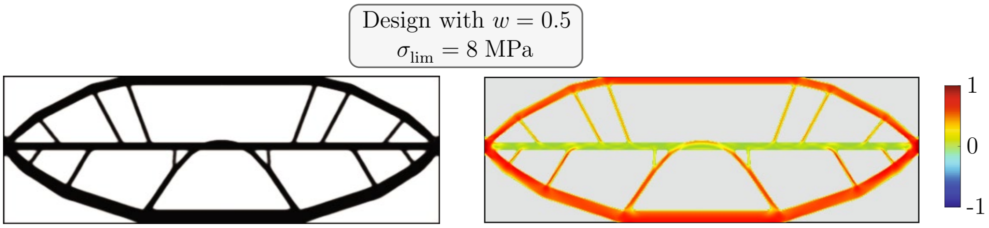

Fig. 20 2D bridge design (left) and von Mises stress field (right) for $\sigma_{\text{lim}} = 8$ MPa

elements. The bridge is made of a linear elastic material with Young's modulus, $E_0 = 27.5$ GPa, and Poisson's ratio and $\nu_0 = 0.2$. For this example, we assume different values of the stress limits in tension (σ^t_{lim}) and compression (σ^c_{lim}) to evaluate their effect on the optimized designs. All results are obtained using a constant weighting parameter of $w = 0.5$ and a filter radius of $R = 2.5$.

The results for three different compression-to-tension stress limit ratios ($\sigma^c_{\text{lim}}/\sigma^t_{\text{lim}}$) and three different stress limits are presented in Fig. 19. Here we wish to highlight a few important observations. First and foremost, the results with a stress limit ratio of 10 and those without a compressive stress limit are identical. Since the materials we consider (e.g., ceramics, concrete, etc.) typically have a compressive stress limit that is much higher than the tensile stress limit, these results illustrate the justification for not including constraints on the minimum principal stress in the main body of this work. In the vast majority of cases the compressive stress constraints would not be active and, consequently, would have little to no effect on the optimized designs. However, for completeness, we also provide the results corresponding to an identical stress limit in tension and compression. In this case, the observed significant change in optimized topology is expected. If the designer wishes to consider a material with a compressive stress limit close in magnitude to its tensile stress limit, then this extension may be useful. Secondly, we note that reducing the tensile stress limit with a stress limit ratio of 10 or greater has removed the under-truss that otherwise develops in an effort to reduce the number of structural members subject to tensile loading. However, reducing the stress limit with a stress limit ratio of 1 does not remove the under-truss from the optimized design, which is likely due to the approximate symmetry of the boundary value problem and stress constraints. Finally, a von Mises stress-constrained result is also provided in Fig. 20 for comparison with the last result shown in Fig. 19, corresponding to equal principal stress limits in tension and compression. As expected, the two optimized designs are quite similar reflecting the tension/compression symmetry of the imposed stress constraints.

Each design example shown in Figs. 19 and 20 required approximately 9 minutes running on a desktop with an Intel(R) Core(TM) i9-10900K CPU @ 3.70GHz and 64GB of RAM.

Appendix 4: Nomenclature

E_0	Young's modulus of solid material
$J^{(k)}(\mathbf{z}, \mathbf{u})$	Augmented Lagrangian function at the k-th sub-problem
N	Number of elements in the finite element mesh
R	Filter radius
$f(\mathbf{z}, \mathbf{u})$	Aggregate objective function
$g_\ell(\mathbf{z}, \mathbf{u})$	Stress constraint of element ℓ
$h_\ell(\mathbf{z}, \mathbf{u})$	Modified stress constraint of element ℓ for the AL method with inequality constraints
p	SIMP penalization parameter
q	Nonlinear filter exponent
α	Parameter used to update the penalty factor, $\mu^{(k)}$
$\bar{\beta}$	Parameter used to control the aggressiveness of the threshold projection function
$\bar{\eta}$	Threshold density value used in the threshold projection function
ϵ	Ersatz stiffness parameter
$\lambda^{(k)}_\ell$	Lagrange multiplier estimator of element ℓ for the k-th AL sub-problem
$\mu^{(k)}$	Quadratic penalty factor for the k-th AL sub-problem
ν_0	Poisson's ratio of solid material
σ^1_ℓ	First principal stress at the centroid of element ℓ
σ_{lim}	Material first principal stress limit
$\mathbf{V}$	Matrix used to obtain J_2 stress invariant in Voigt notation
$\mathbf{A} = \{\Omega_\ell\}_{\ell=1}^N$	Vector of element areas (2D) or element volumes (3D)
$\mathbf{B}_\ell$	Strain–displacement matrix at the centroid of element ℓ
$\mathbf{D}_0$	Material moduli matrix for solid material
$\mathbf{E} = m_E(\mathbf{y})$	Vector of element stiffness parameters

$\mathbf{K}$	Global stiffness matrix
$\mathbf{P}$	Filter matrix
$\mathbf{V} = m_V(\mathbf{y})$	Vector of element volume fractions
$\mathbf{f}$	Global force vector
$\mathbf{k}_\ell$	Stiffness matrix of element ℓ
$\mathbf{u}$	Global displacement vector
$\mathbf{u}_\ell$	Displacement vector of element ℓ
$\mathbf{y} = \mathbf{Pz}$	Vector of filtered densities
$\mathbf{z}$	Vector of design variables
$\boldsymbol{\xi}$	Adjoint vector

Acknowledgements This work was partially funded by the National Science Foundation (NSF) through grant #2105811. We also acknowledge Sandia National Laboratories, a multimission laboratory managed and operated by National Technology and Engineering Solutions of Sandia, LLC, a wholly owned subsidiary of Honeywell International, Inc., for the US Department of Energy's National Nuclear Security Administration under contract DE-NA0003525. OG thanks the endowment provided by the James W. and Joan M. O'Neill Faculty Scholar in Engineering at the University of Missouri. The interpretation of the results of this work is solely that by the authors, and it does not necessarily reflect the views of the sponsors or sponsoring agencies.

Declarations

Conflict of interest The authors declare that they have no conflict of interest.

Replication of results To facilitate replication of the results, the paper discusses the formulation in detail and provides the input parameters for each of the numerical examples. In addition, an IGES CAD file of the design domain for the antenna support bracket is provided to facilitate reproduction of the results for the last example.

References

Bendsøe MP, Kikuchi N (1988) Generating optimal topologies in structural design using a homogenization method. Comput Methods Appl Mech Eng 71(2):197–224

Amstutz S, Novotny AA, de Souza Neto EA (2012) Topological derivative-based topology optimization of structures subject to Drucker-Prager stress constraints. Comput Methods Appl Mech Eng 233:123–136

Bendsøe MP, Sigmund O (2003) Topology optimization: theory, methods and applications. Springer, Berlin. https://doi.org/10.1007/978-3-662-05086-6

Bertsekas DP (1996) Constrained optimization and Lagrange multiplier methods, 1st edn. Athena Scientific, Belmont

Bertsekas DP (1999) Nonlinear programming, 2nd edn. Athena Scientific, Belmont

Bruggi M (2008) On an alternative approach to stress constraints relaxation in topology optimization. Struct Multidisc Optim 36(2):125–141

Cauchy AL (1827) De la pression ou tension dans un corps solide. Exercices Math 2:42–56

Chen A, Cai K, Zhao Z-L, Zhou Y, Xia L, Xie YM (2021) Controlling the maximum first principal stress in topology optimization. Struct Multidisc Optim 63(1):327–339

Cheng GD, Guo X (1997) ε-relaxed approach in structural topology optimization. Struct Optim 13(4):258–266

Sigmund O, Maute K (2013) Topology optimization approaches. Struct Multidisc Optim 48(6):1031–1055

Rozvany GIN (2001) On design-dependent constraints and singular topologies. Struct Multidisc Optim 21(2):164–172

da Silva GA, Beck AT, Sigmund O (2019) Stress-constrained topology optimization considering uniform manufacturing uncertainties. Comput Methods Appl Mech Eng 344:512–537

da Silva GA, Aage N, Beck AT, Sigmund O (2021) Three-dimensional manufacturing tolerant topology optimization with hundreds of millions of local stress constraints. Int J Numer Methods Eng 122(2):548–578

Deaton JD, Grandhi RV (2014) A survey of structural and multidisciplinary continuum topology optimization: post 2000. Struct Multidisc Optim 49(1):1–38

Duysinx P, Sigmund O (1998) New developments in handling stress constraints in optimal material distribution. In: Proceedings of the 7th AIAA/USAF/NASA/ISSMO symposium on multidisciplinary analysis and optimization, vol 1, pp 1501–1509

Giraldo-Londoño O, Paulino GH (2021) `PolyStress`: a Matlab implementation for local stress-constrained topology optimization using the augmented lagrangian method. Struct Multidisc Optim 63(4):2065–2097

Giraldo-Londoño O, Paulino GH (2020) A unified approach for topology optimization with local stress constraints considering various failure criteria: von Mises, Drucker-Prager, Tresca, Mohr-Coulomb, Bresler-Pister, and William-Warnke. Proc R Soc A 476(2238):20190861

Holmberg E, Torstenfelt B, Klarbring A (2013) Global and clustered approaches for stress constrained topology optimization and deactivation of design variables. In: 10th World Congress on structural and multidisciplinary optimization. Orlando, Florida, USA, pp 1–10

Holmberg E, Torstenfelt B, Klarbring A (2014) Fatigue constrained topology optimization. Struct Multidisc Optim 50(2):207–219

Le C, Norato J, Bruns T, Ha C, Tortorelli D (2010) Stress-based topology optimization for continua. Struct Multidisc Optim 41(4):605–620

Lee E, James KA, Martins JRRA (2012) Stress-constrained topology optimization with design-dependent loading. Struct Multidisc Optim 46(5):647–661

Luo Y, Kang Z (2012) Topology optimization of continuum structures with Drucker-Prager yield stress constraints. Comput Struct 90:65–75

Luo Y, Wang MY, Kang Z (2013) An enhanced aggregation method for topology optimization with local stress constraints. Comput Methods Appl Mech Eng 254:31–41

Nocedal J, Wright SJ (2006) Numerical optimization, 2nd edn. Springer, New York

Paris J, Navarrina F, Colominas I, Casteleiro M (2009) Topology optimization of continuum structures with local and global stress constraints. Struct Multidisc Optim 39(4):419–437

Paris J, Navarrina F, Colominas I, Casteleiro M (2010) Block aggregation of stress constraints in topology optimization of structures. Adv Eng Softw 41(3):433–441

Pereira JT, Fancello EA, Barcellos CS (2004) Topology optimization of continuum structures with material failure constraints. Struct Multidisc Optim 26(1–2):50–66

Talischi C, Paulino GH, Pereira A, Menezes IFM (2012a) `PolyMesher`: a general-purpose mesh generator for polygonal elements written in Matlab. Struct Multidisc Optim 45(3):309–328

Talischi C, Paulino GH, Pereira A, Menezes IFM (2012b) `PolyTop`: a Matlab implementation of a general topology optimization framework using unstructured polygonal finite element meshes. Struct Multidisc Optim 45(3):329–357

Wang F, Lazarov BS, Sigmund O (2011) On projection methods, convergence and robust formulations in topology optimization. Struct Multidisc Optim 43(6):767–784

Xia L, Zhang L, Xia Q, Shi T (2018) Stress-based topology optimization using bi-directional evolutionary structural optimization method. Comput Methods Appl Mech Eng 333:356–370

Yang RJ, Chen CJ (1996) Stress-based topology optimization. Struct Optim 12(2):98–105

Publisher's Note Springer Nature remains neutral with regard to jurisdictional claims in published maps and institutional affiliations.